AFRL-AFOSR-VA-TR-2022-0023

Super-resolution imaging in 2D and 3D using the SUPPOSe algorithm based on approximating the imaged object by a superposition of point sources

Oscar Martinez
UBATEC S.A.
GRAL. JUAN JOSE VIAMONTE 577 PISO 6 DEPTO 56
CIUDAD DE BUENOS AIRES, , C1053ABK
AR

11/09/2021
Final Technical Report

Air Force Research Laboratory
Air Force Office of Scientific Research
Arlington, Virginia 22203
Air Force Materiel Command

REPORT DOCUMENTATION PAGE

Form Approved
OMB No. 0704-0188

1. REPORT DATE *(DD-MM-YYYY)*	**2. REPORT TYPE**	**3. DATES COVERED** *(From - To)*
09-11-2021	Final	15 Aug 2018 - 14 Aug 2020

4. TITLE AND SUBTITLE
Super-resolution imaging in 2D and 3D using the SUPPOSe algorithm based on approximating the imaged object by a superposition of point sources

5a. CONTRACT NUMBER

5b. GRANT NUMBER
FA9550-18-1-0470

5c. PROGRAM ELEMENT NUMBER

6. AUTHOR(S)
Oscar Martinez

5d. PROJECT NUMBER

5e. TASK NUMBER

5f. WORK UNIT NUMBER

7. PERFORMING ORGANIZATION NAME(S) AND ADDRESS(ES)
UBATEC S.A.
GRAL. JUAN JOSE VIAMONTE 577 PISO 6 DEPTO 56
CIUDAD DE BUENOS AIRES, C1053ABK
AR

8. PERFORMING ORGANIZATION REPORT NUMBER

9. SPONSORING/MONITORING AGENCY NAME(S) AND ADDRESS(ES)
AF Office of Scientific Research
875 N. Randolph St. Room 3112
Arlington, VA 22203

10. SPONSOR/MONITOR'S ACRONYM(S)
AFRL/AFOSR IOS

11. SPONSOR/MONITOR'S REPORT NUMBER(S)
AFRL-AFOSR-VA-TR-2022-0023

12. DISTRIBUTION/AVAILABILITY STATEMENT
A Distribution Unlimited: PB Public Release

13. SUPPLEMENTARY NOTES

14. ABSTRACT
A new method has been developed that opens the field of super-resolution microscopy to standard equipment and single shot experiments. In this manner fast events can be traced with high spatial resolution never available before. This new method, SUPPOSe (for Superposition of point sources) is based on the assumption that the target object to be retrieved (hidden by the resolution of the instrument) can be represented as the superposition of virtual sources of the same intensity. In this manner the ill posed mathematical problem of inverting the convolution (deconvolution) is converted to a well posed problem and a resolution beyond the instrument limitation can be achieved. The limits to this deconvolution are placed by the noise figure of the measurement and the precision with which the instrument response function is determined.

The method is thoroughly tested using synthetic images and is validated with the super-resolution of intracellular structures such as mithocondria, actin filaments and microtubules. An extension to scattering images (non fluorescent) is presented and several improvements in the algorithm are described including the use of neural networks for image denoising before processing with SUPPOSe.

15. SUBJECT TERMS

16. SECURITY CLASSIFICATION OF:			**17. LIMITATION OF ABSTRACT**	**18. NUMBER OF PAGES**	**19a. NAME OF RESPONSIBLE PERSON**
a. REPORT	**b. ABSTRACT**	**c. THIS PAGE**			BRADFORD BARRETT
U	U	U	SAR	38	**19b. TELEPHONE NUMBER** *(Include area code)* 588-8442

Grant Number
FA9550-18-1-0470

Super-resolution imaging in 2D and 3D using the SUPPOSe algorithm based on approximating the imaged object by a superposition of point sources

PI: Oscar Eduardo Martínez

PERIOD OF PERFORMANCE
15 AUG 2018 through 14 AUG 2021

Table of Contents

List of figures

Summary
A new method has been developed that opens the field of super-resolution microscopy to standard equipment and single shot experiments. In this manner fast events can be traced with high spatial resolution never available before. This new method, SUPPOSe (for Superposition of point sources) is based on the assumption that the target object to be retrieved (hidden by the resolution of the instrument) can be represented as the superposition of virtual sources of the same intensity. In this manner the ill posed mathematical problem of inverting the convolution (deconvolution) is converted to a well posed problem and a resolution beyond the instrument limitation can be achieved. The limits to this deconvolution are placed by the noise figure of the measurement and the precision with which the instrument response function is determined.
The method is thoroughly tested using synthetic images and is validated with the super-resolution of intracellular structures such as mithocondria, actin filaments and microtubules.
An extension to scattering images (non fluorescent) is presented and several improvements in the algorithm are described including the use of neural networks for image denoising before processing with SUPPOSe.

Introduction

In the last decades several super-resolution methods have been developed to overcome the diffraction limit in optical microscopy that have drawn great attention and three researchers received the nobel prize in 2014. In all the cases the techniques rely in the detection of fluorescence from appropriate molecules native or added to the specimen under study. The super-resolution was achieved either by means of some nonlinearity and ingenious tricks as done in STED [1,2] or by localizing individual molecules one at a time as they are switched on and off purposely as in PALM or stochastically as done in STORM [3, 4, 5]. STED is a scanning technique using sophisticated lasers and PALM and STORM require the acquisition of hundreds or thousands of images. None of the above mentioned methods allows the acquisition of non-fluorescent images with super-resolution nor a rapid single image acquisition.

The problem to be solved is finding the signal source *R(x)* that in the image is convolved with *I(x)*, the instrument response function or Point Spread Function (PSF) and with the addition of backgropund *B(x)* and noise $\eta(x)$ yielding a detected signal given by:

$$S(x) = R * I(x) + \eta(x) + B(x) \quad (1),$$

Several deconvolution numerical methods have been developed to invert the problem posed by equation 1 with great success in recovering 3D information blurred from out of plane fluorofores [6-13]. A recent review can be found in [14] where it becomes obvious that no super-resolution is achieved. A deconvolution method with super-resolution known as compressed sensing [15-21]; has attracted great attention and has been added to the single molecule localization techniques mentioned before to increase acquisition speed, reducing the number of frames from thousands to several hundreds [19,; 22-24], but still no single image reconstruction has been possible.

The method proposed in this project is based on transforming the problem posed in equation 1 to the approximation of the source function *R(x)* by a superposition of N point sources of equal intensities, converting the question of finding the intensity *R* for each position x to finding the positions x for each source. The method has been named SUPPOSe (for SUPerposition of POint Sources) and it must be distinguished from the prior localization techniques as described in the figure 1

In the first row of Figure 1 the localization concept is presented. The left image is the PSF of the microscope and a point source superimposed in the same frame. The second image shows how a localization algorithm would retrieve the position of the source with a certain error related to the uncertainties of the method, and in the third frame the same problem recovered with the SUPPOSe algorithm, where the answer is a cloud of sources distributed around the original source with a dispersion related to the uncertainty of the method. The second line shows a different case where the source is a continuous distribution of sources (Figure 1-E) that after convolving with the PSF yields the image obtained in Figure 1-D. In Figure 1-E a dot is shown indicating the result that would be retrieved if a localization algorithm is used (a single source is found). In Figure 1-F the result of

applying the SUPPOSe algorithm is presented, showing a cloud of point sources that resembles the original distribution of Figure 1-E.

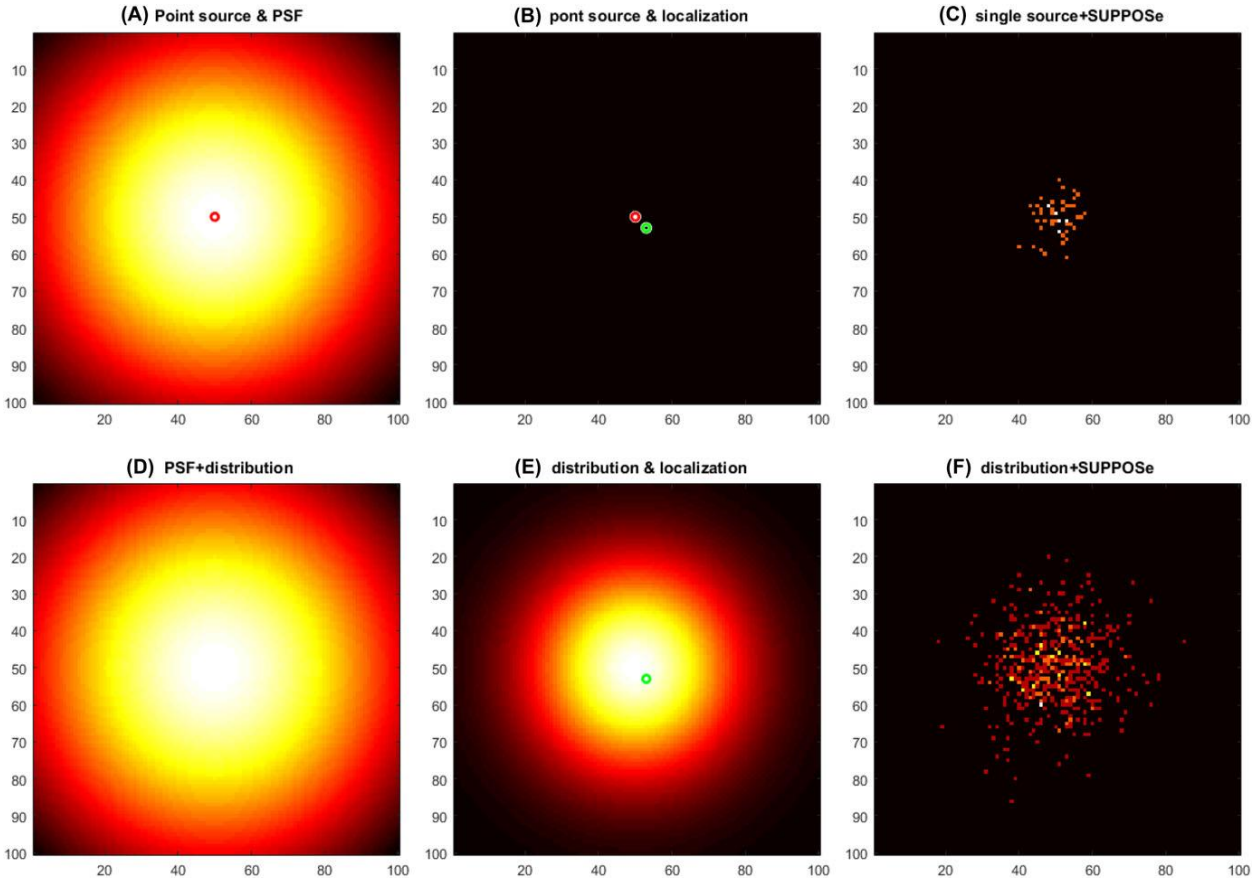

Figure 1 Schematics of the method. First row, a single source, second row, a continuous distribution of sources. (A) Red circle: point source. Image: measured result due to convolution with the PSF. (B) Red circle: original point source. Green circle: typical result from a localization algorithm. (C) Typical result with the SUPPOSe method: a cloud of virtual sources grouped around the actual source. (D) Image: measured result due to convolution of a distribution of sources with the PSF. (E) Distribution of sources not broadened by the PSF and green circle: result of a localization algorithm. (F) Result after SUPPOSe: a cloud of virtual sources distributed reconstructing the original source distribution.

In the following sections the method is described, several improvements are presented to increase the processing speed or admit a look up table as the source of information regarding the instrument response function. An annalitycal bound to the accuracy and resolution of the method is presented and further exploration in this issue is performed numerically with synthetic images and validated with real images of intracellular organelles. Extension of the method to edge detection in 2D and 3D are presented and a neural network approach is shown to allow a reduction in the noise to improve the algorithm performance. The method is shown to work also with non-fluorescent images (incoherent scattering).
As a result of this work 2 PhD thesis were cpompleted, by Micaela Toscany and Guillermo Brinatti Vazquez. The papers highlighted in bold in the reference list are those from the group in the frame of this project.

Methods, Assumptions and Procedures

The method developed called SUPPOSe consists on representing the target function *R(x)* of equation 1 as a superposition of *N* virtual point sources of equal intensity *α* . Now the problem of finding the intensity *R* for each position *x* is converted into finding the positions of the *N* sources. Hence, the approximate solution *R'(x)* would result:

$$R'(x) = \alpha \sum_{k=1}^{N} \delta(x - a_k), \quad (2)$$

where a_k are the positions of the sources.
In figure 2 a flow diagram of the algorithm is presented. A genetic algorithm is used to determine the best positions of the N sources used for the fit. The comparison with the measurement is made by convolving the proposed solution R´ with the instrument response function or Point Spread Function I(x) generating a synthetic image S´(x) to be compared with the measured one S(x). The fitness criterion is the chi square:

$$\chi^2 = \sum_{i=1}^{n} (S(x_i) - S'(x_i))^2 \quad (3)$$

The sequence starts with the image to be processed. An initial choice for *α* (intensity of the sources) and the number of sources is made (see details in [25]). An initial family for the genetic algorithm is created by successively locating a source at the most intense point of the image and subtracting the contribution of that source from the image. Some randomness is added by shifting the positions of the sources by a random number of the order of the PSF standard deviation. In this manner the number of individuals of the initial family is generated. The genetic algorithm is executed and with the solution obtained the optimal value N_{op} is determined. If the value *N* used is not close enough to this optimal value the procedure is repeated with the new *α* and *N*. The result can be presented in two ways: one is to define a new pixel we call superpixel and display a histogram of the number of sources that fall within each pixel, the other option is to convolve the sources obtained with the shape of the bead used to determine the PSF.
A full analytical derivation of the method and the study of quality of the fit is given in [25], where it is proved that the method circumvents the ill posed problem if the direct deconvolution, becoming a well posed problem that converges close enough to the actual objective function R.

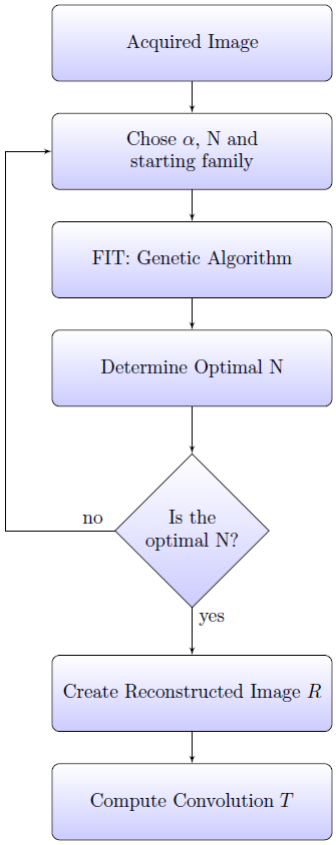

Figure 2: flow diagram of the algorithm.

Several different strategies were performed according to the nature of the task. They include the construction of synthetic images of different character to test the algorithm and the eventual changes so that the ground truth to compare the result is available. Typically the artificial structures consisted in parallel lines at distances lower than the resolution of the instrument, measured by the width of the synthetic PSF. The test for the increase in speed with parallel computing using graphical processing units (GPUs) were performed using synthetic images.
Part of the validation included the measurement of intracellular organelles with super-resolution. The cell targeted structures were labeled with fluorescent molecules, and this was done for F-actin filaments, microtubules and mitochondria. Fluorescent beads tens of nanometers in diameters were used to measure the PSF. This was done by fitting the measured data with specific functions. The data were originated by the measurement of tens of beads that were localized and concentered to make a final fit with all the beads together [25].

Results and Discussion

I. Hardware construction

For the fluorescent microscope experiments an Olynmpus IX71 system was used with LED illumination sources. In order to increase the oversampling

needed for the SUPPOSe algorithm an additional 2x telescope was added between the camera port and the camera as shown in figure 3. The first lens of the telescope was mounted in a motorized translation stage and used as a focusing unit, avoiding the use of the motorized objective as a way to generate a z-stack for 3D deconvolution. The reason for this is that it avoids the possible deformation of the sample when working with a oil immersion objective. The detection was performed using an Andor Zyla 5Mpxls CMOS camera with a very low dark count rate and readout noise and 16bit dynamic range. The pixel size at the sample results: 3250nm/M where M is the microscope magnification (depending on the objective and the additional 1.6x lens goes between 10 and 96)..

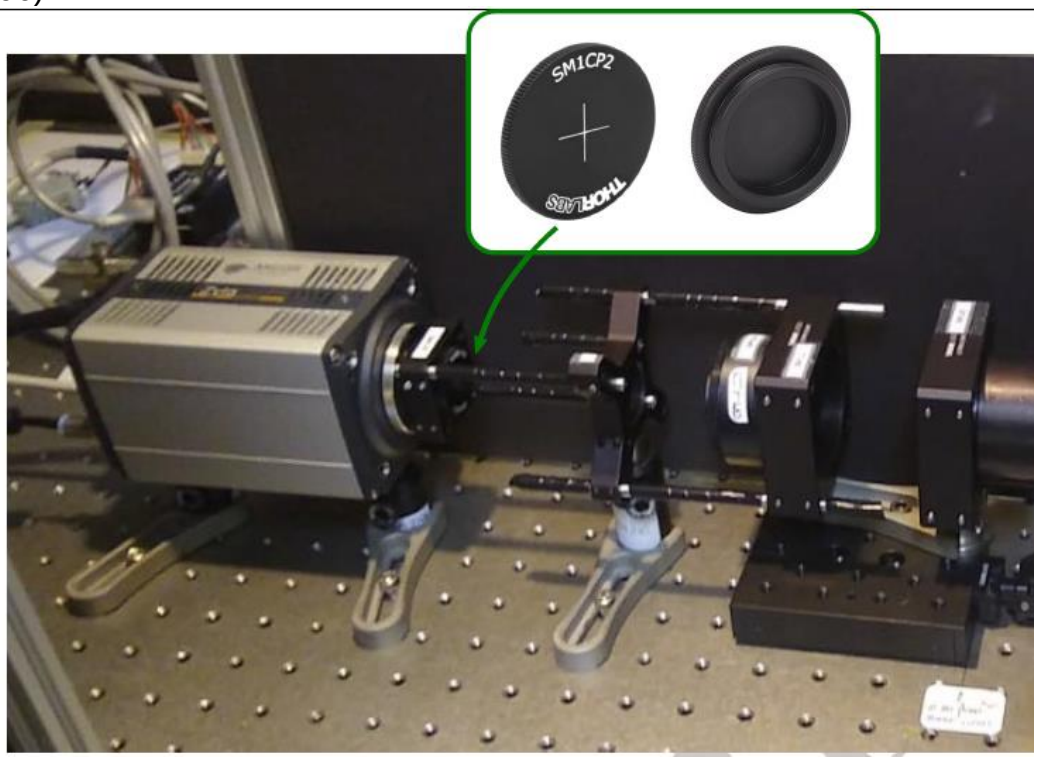

Figure 3: 2x telescope added to the epi-fluorescence microscope and camera.

For multiphoton microscopy a specific microscope was designed and built with a configuration shown in Figure 3. A Ti:Sapphire ultrashort pulse laser was built and used as illumination source. The laser is sent towards the sample and is scanned across the sample surface and the complete image is recorded using two photon counting units with adequate filters for 2 channel simultaneous detection. A prism compressor is placed in the sample arm to compensate for the time delay dispersion arising from the optical material in the beam path. A LED and a camera are also installed to obtain a wide filed image of the sample.

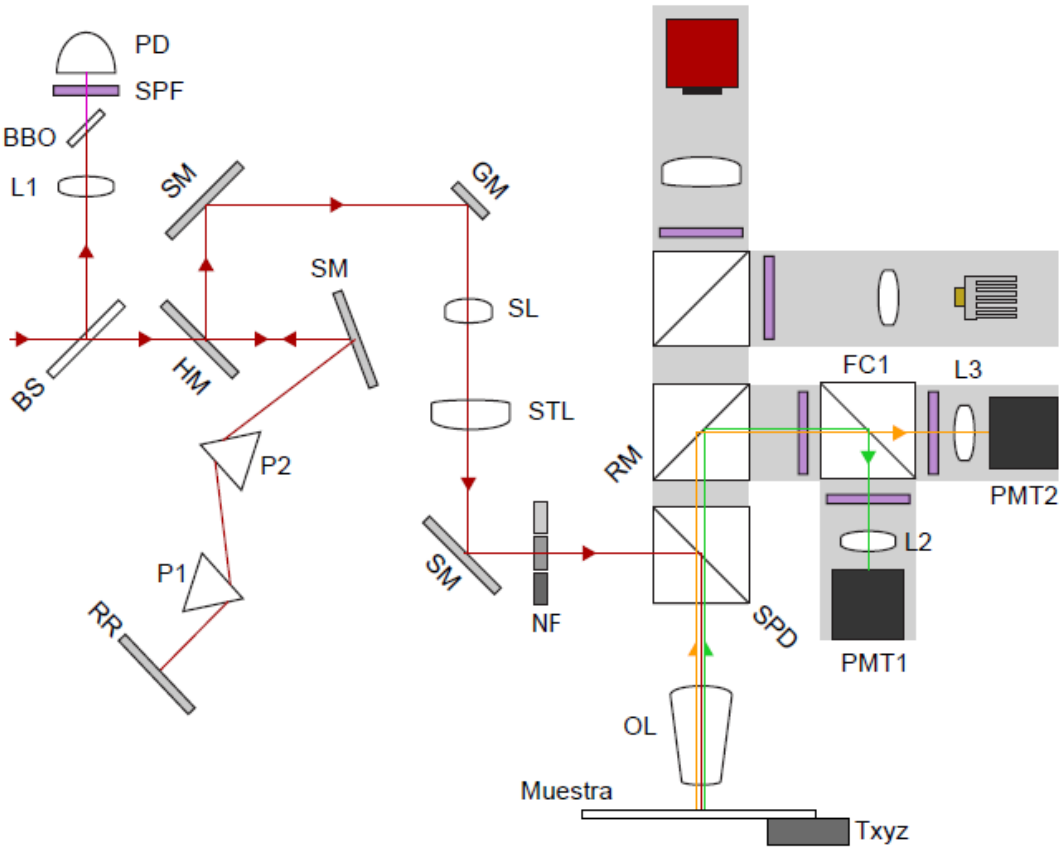

Figure 4. Microscope for multiphoton imaging.

II. First results with fluorescent microscopy

To validate the method two different types of experiments were carried out using the fluorescent microscope described above. The first one was to generate artificially synthesized images with known ground truth to be able to compare the retrieved data with the actual source. The second one was to measure a sample with objectives of different resolutions and use the best objective as the ground truth to test the retrieval from the image with the lesser resolution. Finally images with our highest available resolution were acquired to show the possible performance of the algorithm.

In Figure 5 the case of synthesized images is shown. The image was generated assuming two parallel lines separated 144nm as the source(Figure 5-a). The artificial image was generated by convolving the source with a typical PSF for our microscope and adding noise similar to that measured for our camera.

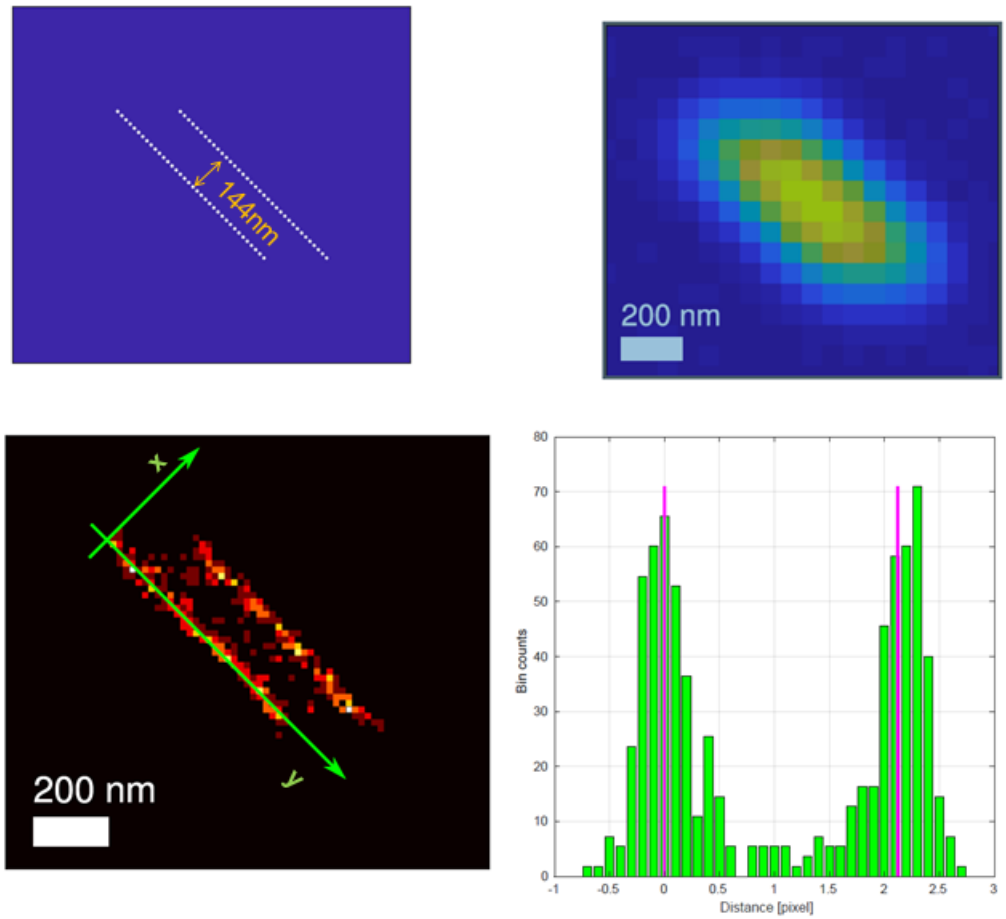

Figure 5-a. Artificial object: 142 sources in 2 parallel lines 144nm apart. -b. Synthetic image using the camera noise and dynamic range and the PSF for our 1.3NA objective.
c. Histogram of the recovered positions using 450 sources. –d. Histogram of the position of the sources projected along the x axis of (c). σ=20nm for each lobe.

Figure 5-c shows the reconstruction obtained after applying the algorithm and in Figure 5-d the histogram of the position of the sources projected along the lines showing a standard deviation of 20nm around the lines. The algorithm provides an estimation of the optimum numbers of virtual sources that should be used to optimize the spatial resolution achieved. For this particular case the predicted optimum was N=415 and an increase in resolution as high as 5 was achieved. More details are presented in [25].

A low magnification objective (10x, NA=0.3) was used for the measurement and retrieval and a higher magnification objective (40x, NA=0.95) was used to determine a reliable ground truth. In Figure 6, a sequence is presented for Bovine pulmonary artery endothelial cells (BPAEC) where mitochondria were stained with MitoTracker Red CMXRos. The zoomed region of interest appeared blurred to the point where the structure revealed by the high numerical aperture (NA) objective appeared to be completely lost. After reconstruction with SUPPOSe using 2156

sources in Figure 6(d), the fine structure is mostly recovered. As discussed in detail in [25] the reconstruction recovered the desired features with two types of distortions that are the merging of two parallel lines into a single intermediate line, and the Y bifurcation where the two branches of the Y are merged into a prolonged stem until the separation between branches is large enough for an adequate reconstruction. The theoretical bound for the resolution obtained was700nm,larger than the obtained resolution of around 500 nm (a twofold improvement as compared with the 1100 nm resolution of the objective at this wavelength).

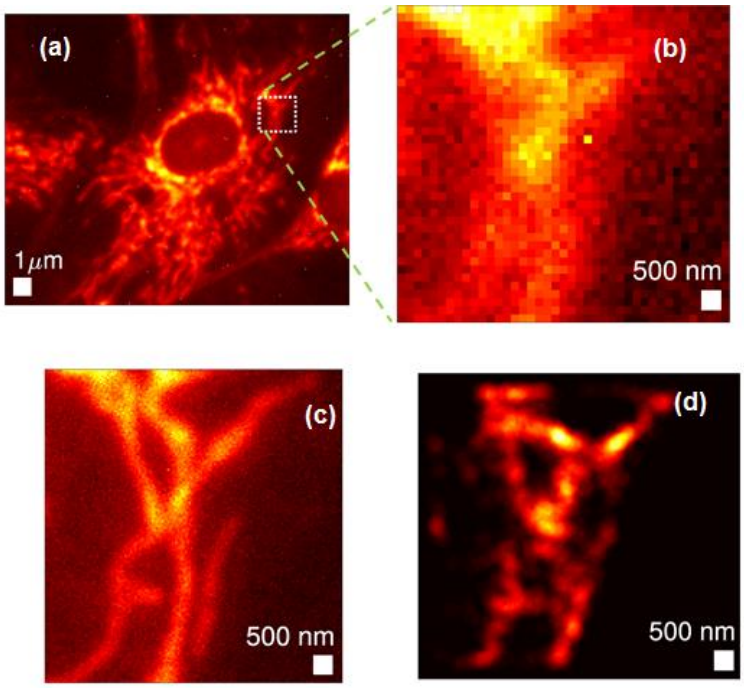

Figure 6. BPAEC:mitochondria stained with MitoTracker® Red CMXRos imaged with the 10x objective. –b. ROI for comparison. –c. Image obtained with the 40x objective. –d. Reconstructed image using SUPPOSe

In Figure 7, the original image and the reconstructed one of labeled microtubules are displayed. Using a NA=1.33 objective and the emission peak at λ = 530 nm, the resolution was 200 nm and the pixel size 44 nm. The predicted bound for the resolution of the reconstruction from SUPPOSe is 130 nm. The reconstruction shows a particular relevant feature, a 125 nm diameter loop with a clearly resolved loophole and a crossover that coincides with the brightest region of the original image. From the predicted resolution, one can ascertain that the loop is a real feature and not a reconstruction artifact. Lower along the strand, a splitting in two parallel strands located 90 nm apart appears. As was discussed before, even though the feature has better resolution than the predicted bound, splitting of a line in two is not an expected distortion but conversely, the fusion of two lines into one is a normal deformation. Hence, this splitting can also be attributed to a real feature. The width variation along the strand, which is below 55 nm, is clearly an artifact. Again, the resolution obtained is about a factor of 2 better than the predicted bound, in the order of 60 nm.

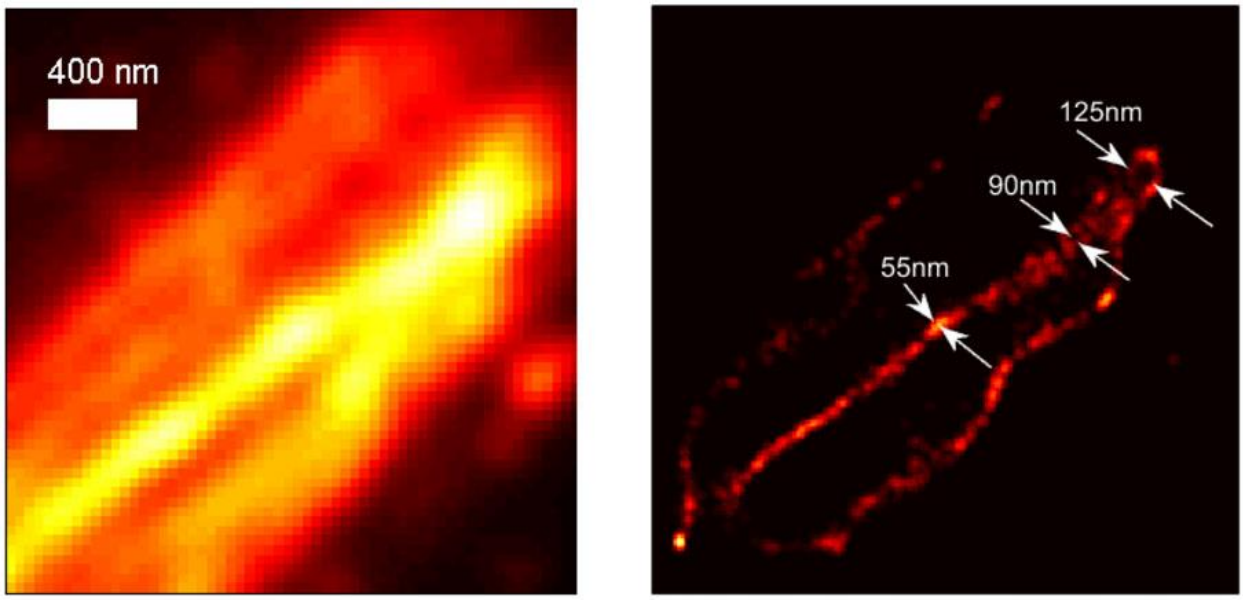

Figure 7. BPAEC anti-bovine-tubulin mouse monoclonal 236-10501 in conjunction with BODIPY FL goat anti-mouse IgG antibody is labeling microtubules-a.wide field. b. Reconstructed image using SUPPOSe

The results presented in this report are only the most significant examples. More cases and details can be found in [25, 26].

III. Improving the algorithm

a)Speeding with GPUs

Processing with a CPU resulted in execution times extremely long (several hours per frame). Tracking down each component of the process it was established that most of the computation time was taken by the calculation of the χ^2. Figure 8 shows the computation time scaling with the size of the image, the number of virtual sources and the number of individuals per generation in the genetic algorithm. It can be seen that as long as the system does not run out of memory the scaling laws are as follows: quadratically with the frame length, and linearly with the number of sources and population. But it should be considered that the number of sources will scale at least linearly with the side of the frame, yielding a fourth power scaling of the execution time with the frame side.

To speed the process the program running in Matlab in a CPU was reprogrammed to run under Python in a GPU.

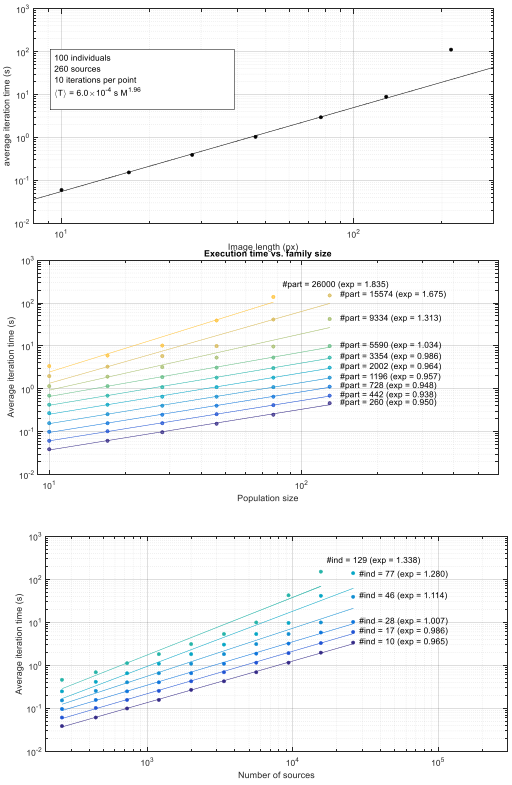

Figure 8. Scaling of the execution time. a: with frame side length, b. with population size, c. with number of virtual sources.

In Figure 9 the comparison between processing with the CPU and the GPU is presented for two different frame sizes plotted as a function of the number of virtual sources.

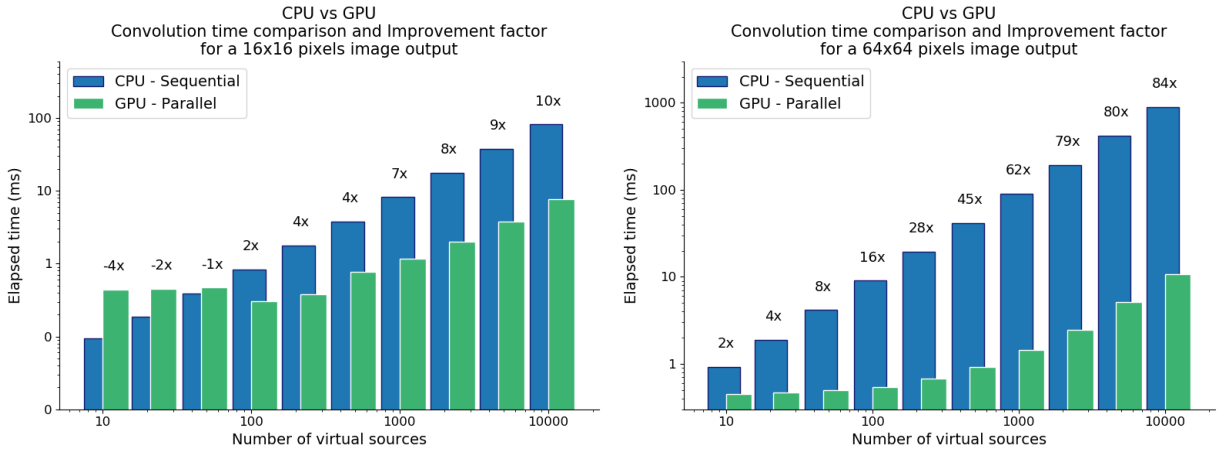

Figure 9. Comparison between CPU and GPU processing.

In Figure 10 a plot of the `rocessing speed for both CPU and GPU processing is shown and the improvement factor for the case of 10000 virtual sources is presented as a function of the image size. It can be seen that parallel processing in the GPU yields a constant processing time until the GPU runs out of available nuclei, and from there on the time grows in a similar maner as with the CPU

yielding a constant improvement factor of 80. Increasing the GPU size will result in even higher increase in the improvement factor.

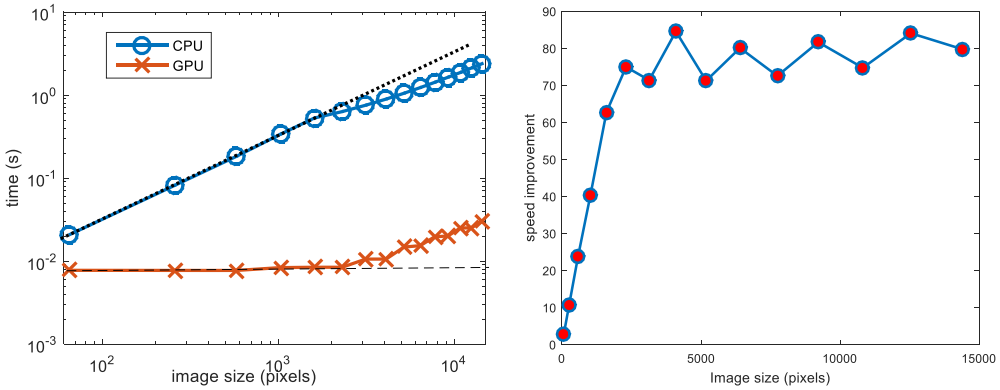

Figure 10: a. processing time vs. image size for CPU and GPU. B. Improvement factor vs, image size for N=10000.

b)Solving artifacts

In this section we describe the advances in the implementation of the algorithm to gain resolution and remove artifacts due to the presence of fluorescent molecules close enough to the image frame boundary. The algorithm was modified removing the invariant used before given by the product of the flux of the virtual sources times the number of virtual sources, and replacing it by a new invariant given by the total flux within the frame, thus allowing the location of virtual sources outside the frame but contributing to the signal inside the frame. This correction becomes particularly relevant because of the need to tile the frame to speed the processing. More tiles are used implying more molecules near the edges of the tile, inside or outside, that contribute in a fractional manner in the total intensity within the tile.
To account for the near boundary sources the synthetic image S' in eq. 3 is replaced by

$$\bar{S}(x) = \alpha \sum_{k=1}^{N} \tilde{I}(x - a_k) - \frac{\alpha}{n} \sum_{i=1}^{n} \sum_{k=1}^{N} \tilde{I}(x_i - a_k) \qquad (4)$$

To test the method we start with the image synthesized before consisting in two parallel straight segments 144 nm apart convolved with a Gaussian PSF, with noise and background added. The parameters used to synthesize the image were selected to simulate the experimental conditions of a widefield fluorescence microscope. The pixel size is 68 nm and the PSF width is 97.6 nm. This is similar to the resolution obtained with emitted light at a wavelength of 520 nm and a microscope objective of numerical aperture 1.3 (figure 11.a).
In Figure 11b, the SUPPOSe reconstruction for N=400 is presented. But, if we cut this image in two sub-images where on each image we use N=200 we obtain the results of Figure 11c. We can see that the artifacts on the boundary here are

catastrophic. Instead when we apply the modified SUPPOSe method we obtain the results of Figure 11d.

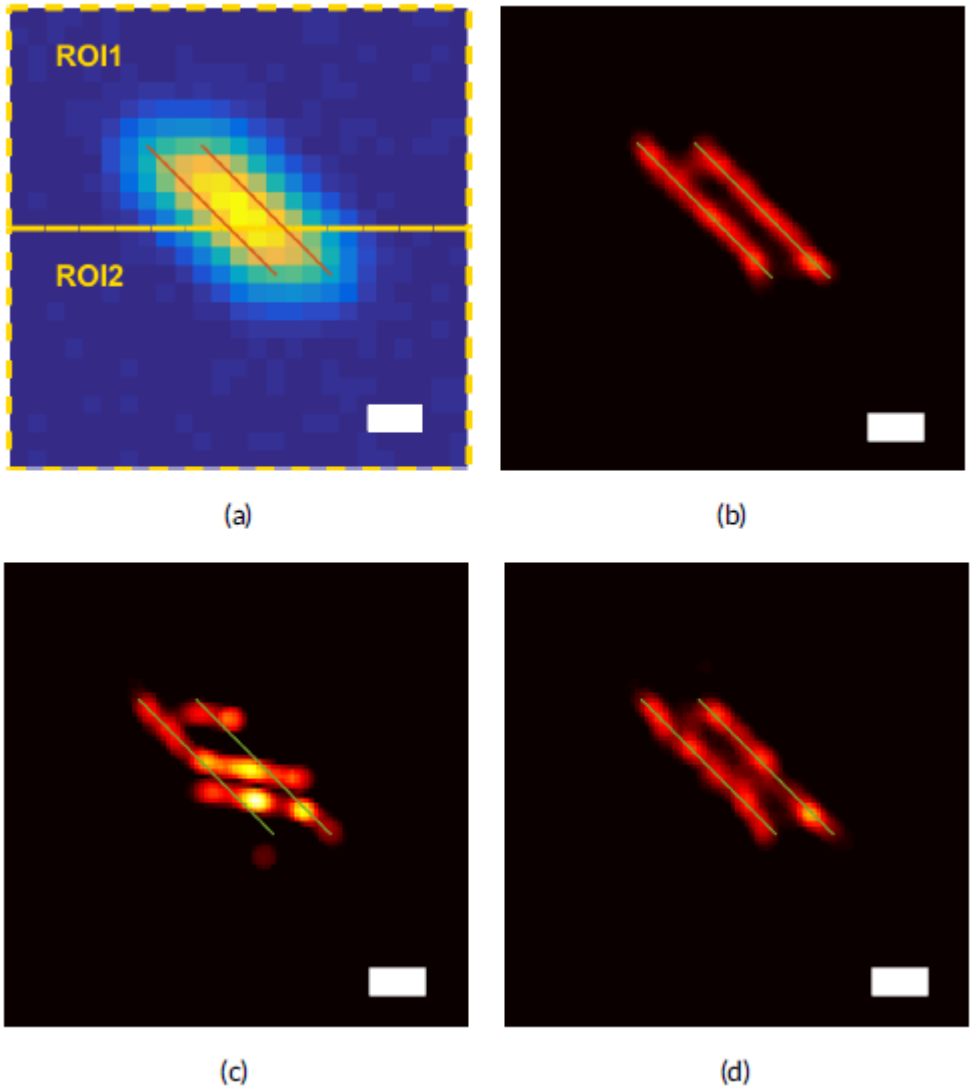

Figure 11. (a) Graphic of the source R (the two parallel orange straight segments, each generated by 71 sources spaced .:9.6 nm) and the synthesized image S obtained after convolving R with the PSF, adding the noise and the background. (b) After SUPPOSe. (c) After applying SUPPOSe to each tile of (a). (d) After applying the modified SUPPOSe to each tile of (a). Solutions convolved with a .50 nm circle. (Scale bar .• 200 nm)

Another important structure formed by the actin protein are the f-actin filaments that are part of the cytoskeleton of cells. We process images of f-actin present in the endothelial cells of the bovine pulmonary artery (BPAEC). Figure 12 shows the results obtained from processing a specific region of the sample. We split the original image into two tiles and processed them separately with the two SUPPOSe methods. The results obtained are shown in the figures 12b and 12c. Artifacts generated by the original SUPPOSe method at the boundaries of the tiles distort information present in the whole region, as can be seen in the regions boxed in green and blue in the figures 12b and 12c. Observe for example, that in Figure 12b

the region corresponding to the dash green box may be confused with a structure of two straight segments. With the modified SUPPOSe the presence of a diferent type of structure in that region can be appreciated. Instead in the yellow box a structure that appears to be a boundary artifact is found that with the modified method it can be ascertained that it is the actual structure.

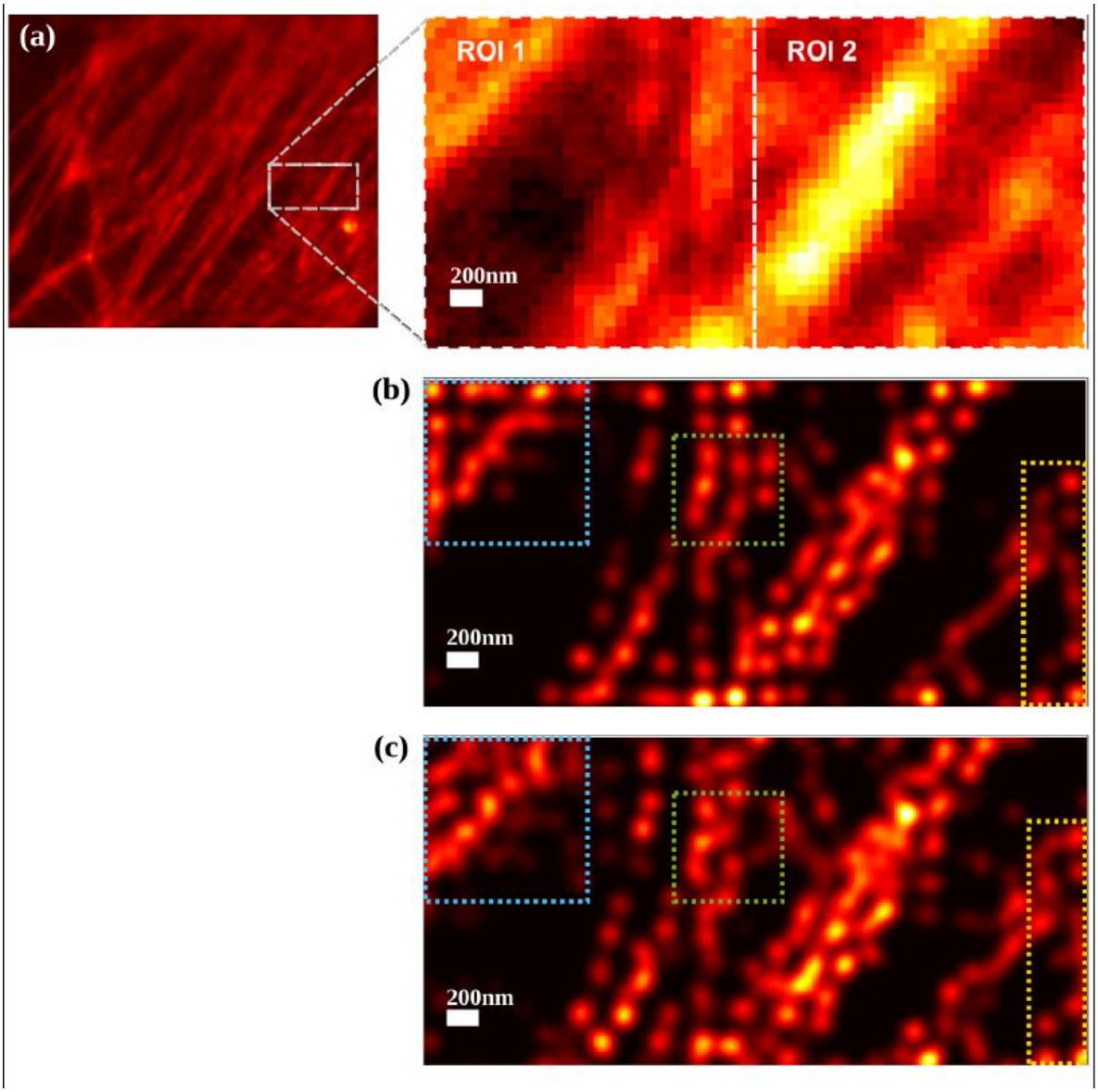

Figure 12. F-actin present in a bovine pulmonary artery endothelial cell and SUPPOSe solutions. (a) The original image was divided into two tiles, each region was processed separately. (b) After applying SUPPOSe. Regions corresponding to the dashed green and light blue boxes respectively: the structures consist on parallel lines to the boundaries. (c) After applying the modfied SUPPOSe. New type of structures appear on the same mentioned regions. Yellow box: a structure that appears to be boundary artifact was the actual structure. Scale bars 200 nm. Solutions convolved with a gaussian function of sigma 50 nm.

For more details see [27]

c)Alternative fitness functions

In this section we show an alternative objective function for optimizing the source positions in the SUPPOSe algorithm. The genethic algorithm (GA) provides similar performance as the original but without the necessity of adjusting α, thus saving an optimization step that will be used in future work for performing blind deconvolution in cases where the PSF is not well known. It will also provide a better scenario for computing 3D images with a PSF that must be defined by a table of values instead of an analytical function.
We define the normalized covariance function as

$$|Cov(A) = 1 - \frac{\sum_{i=1}^{M}\sum_{k=1}^{N} I(\mathbf{x_i} - \mathbf{a_k})S(\mathbf{x_i})}{\sqrt{\sum_{i=1}^{M}\left(\sum_{k=1}^{N} I(\mathbf{x_i} - \mathbf{a_k})\right)^2}\sqrt{\sum_{i=1}^{M} S(\mathbf{x_i})^2}}, \quad (5)$$

where x_i is the i-th pixel location. Due to its normalization, this objective function is independent of the intensities α and thus the LLS regression is no longer necessary.
To test the method, we started with a simulated PSF and a synthesized image similar to the ones proposed in [1]. The sample consisted in two parallel straight lines 2.12 px apart, each one made up from 71 point sources separated 0.14 px from each other (see figure 2 (a)). The true source distribution was convolved with a $2\sigma_{psf}$ = 2.87 px width Gaussian PSF, and then a mixture of Poisson and Gaussian noise patterns was added. We tested each objective function by performing 45 runs of the algorithm, each run consisting in 3 × 10^4 iterations starting from the same initial population (see figure 2 (b)) of size m = 100 and elite size n_e = 10. In all cases, the parameters of the GA (named as in [25]) were: $scale\_fit$ = 10, p = 40 %, n = 20 %, $\rho 0 = 0.01 \cdot \sigma$.

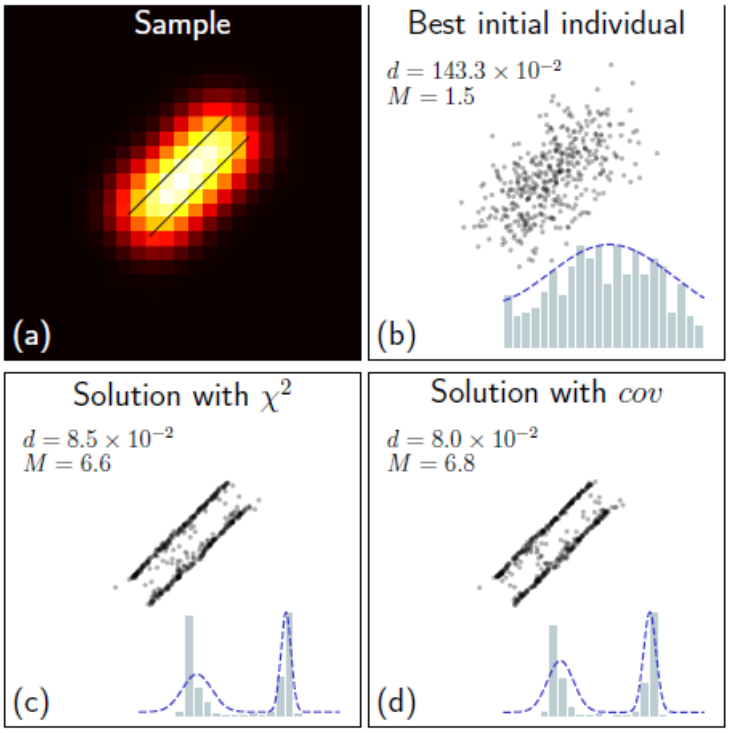

Figure 13: (a) synthesized image S (x) and true sources R(x). (b) Best individual in the initial family. (c) and (d) solutions for f = χ2 and f = Cov respectively. Insets show an histogram of source positions and the adjusted source distribution.

A maximum likelihood estimation allowed us to measure both the center and the width of the reconstructed lines by assuming a mixture of two Gaussian distributions for the source positions along the direction transverse to the lines (see insets of figure 1 (b), (c) and (d)). From these parameters we measured the line displacement d as the average distance from each line to its true center, and the resolution improvement factor M as the ratio of the PSF width to the average line width.

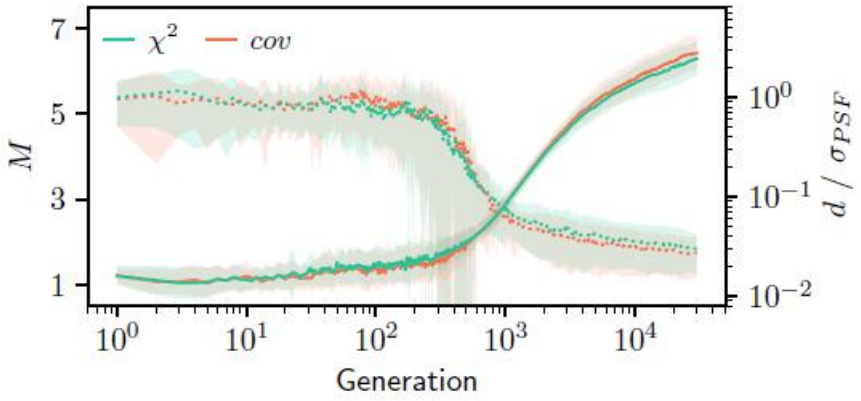

Figure 14: Evolution of M (solid line, left axis) and d (dotted lines, right axis) for each objective function during 3 × 10^4 iterations of the algorithm. Mean values (lines) ± a standard deviation (shaded areas) for 45 runs are shown.

The evolution of M and d for each objective function is shown in figure 3. For both objective functions, the reconstructed lines became distinguishable from each other around iteration 500, when the line bias decreased below σ . The improvement factor is also similar in both cases, achieving values of M = 6.3 ± 0.4 for f = χ2 and M = 6.4 ± 0.4 for f = Cov. Figure 4 shows histograms for the adjusted parameters at the end of the runs, from which we can see that the statistics obtained for both objective functions are indistinguishable from each other.

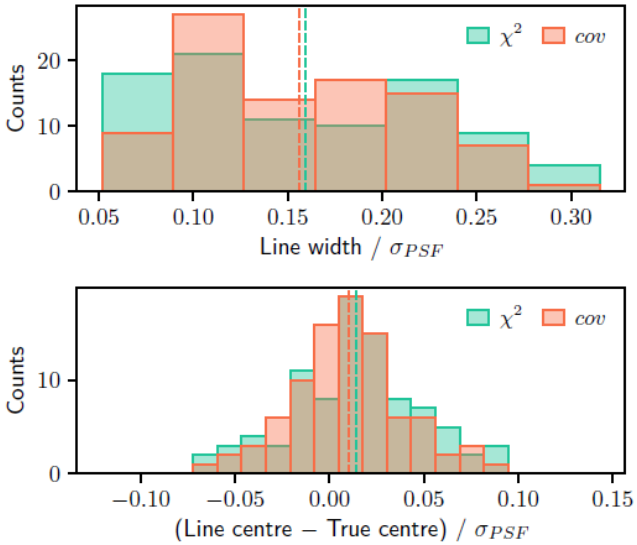

Figure 15: Histograms of the line width (top) and line bias (bottom) normalized by σ_{PSF} at the end of all 45 runs. Dashed lines indicates the mean values

For more details see [28]

d) Fourier space processing

From the alternative fitting function shown before a new possibility of increasing the speed appears, as the covariance is invariant if worked in the Fourier space and in this case the convolution is converted into a product, the computation can be significantly speeded at the expense of discretizing the space. This is because in the direct space the sources can be located at any arbitrary position not conditioned by the pixilation of the image, but to perform efficiently the Fourier transform a discretization is mandatory. This discretization was performed at a much smaller grid than the acquisition sampling mesh.
It was necessary to compare the two methods and for this purpose our standard two line synthetic sample was used. Both methods were run in a multicore CPU under a matlab code. The parameters used are displayed in table 1 and the results and comparison is made in table 2. Figure 16 shows one particular fit to illustrate the quality of the method. From the table it can be concluded that the accuracy of

the FFT version is limited by the pixilation used for the calculation and that the random kicks must be larger because otherwise the sources are not kicked out of the pixel. The speed showed a fantastic improvement as for 10 thousand iterations the SUPPOSe computation took 4 hours while the SUPPOSe_fft took only 13 minutes.

	PSF width in pixels	Image size	Distance between lines
SUPPOSe	1.425	32x32	1.48σ=2.12
SUPPOSe_fft	5.7	128x128	1.48σ=8.43

Table 1. parameters used for the fit

	SUPPOSe	SUPOSe_fft
No noise, random kick= 0.1	0.8/0.86	0.98/0.86
Noise, random kick= 0.1	0.905/0.9	1.03/0.86
No noise, random kick= 0.01	0.51/0.61	2/1.4
Noise, random kick= 0.01	0.74/0.86	2.08/1.44

Table 2. results with both methodst. Data correspond to mean / standard deviation of the accuracy

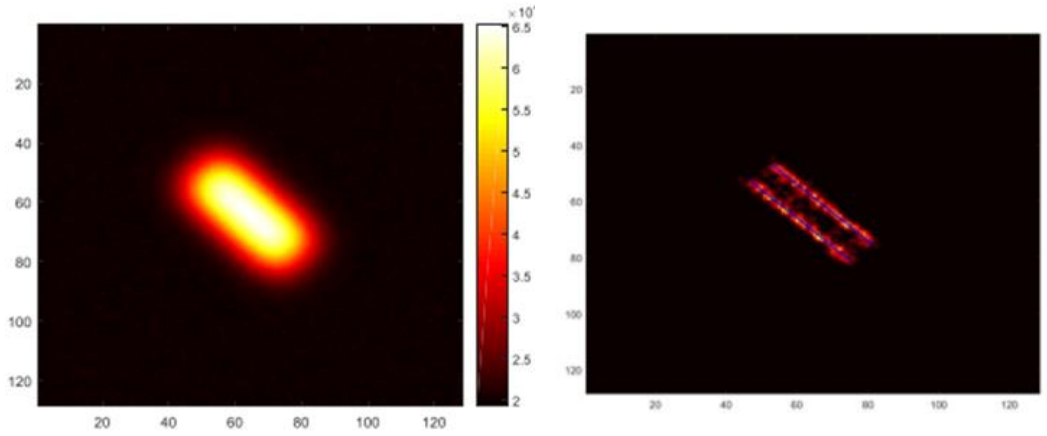

Figure 16: Left, synthetic image from two lines Right: reconstruction using SUPPOSe_fft

This work has not been published yet.

IV-Resolution, precision and accuracy

The SUPPOSe algorithm was tested with synthetic images in intensity ranges similar to those found in a conventional fluorescence experiment, the resolution value obtained depends on the level of noise present in the image. Performing

simulations with a wide field resolution of 236 nm under standard signal to noise ratios, a SUPPOSe resolution of 75 nm with an accuracy of 20 nm and a precision of 10 nm (based on the distance measure) is shown to be possible. We observe that the method, despite being very robust against high frequency noise, is conditioned by the structure of the low frequency noise, tending to over fit it when the signal-to-noise ratio in the image is low. In the case of the experimental images, comparing the solutions with each other we obtain a precision value of 37 nm that is within the range estimated from synthetic images for the same noise levels. As a final remark it can be suggested as a good practice using SUPPOSe to take repeated images in a typical experimental situation to quantify the precision for further similar experiments

In figure 17 the retrieved structures are shown for different distance between lines and different noise levels. The noise figure is defined as

$$NF = \max\left[\frac{roi - background}{\sigma_{Noise}}\right] \qquad (6)$$

where roi is the image to be processed with SUPPOSe. The background is a constant value that is subtracted from the image, for the case of synthetic data this value is known and for experimental images it is estimated by extracting the mean value of a region in the image that does not have signal information. The value σ_{Noise} is the standard deviation of the noise or an estimate thereof. The operation is performed pixel by pixel and max[.] is a function that returns the maximum element value in the resulting array.

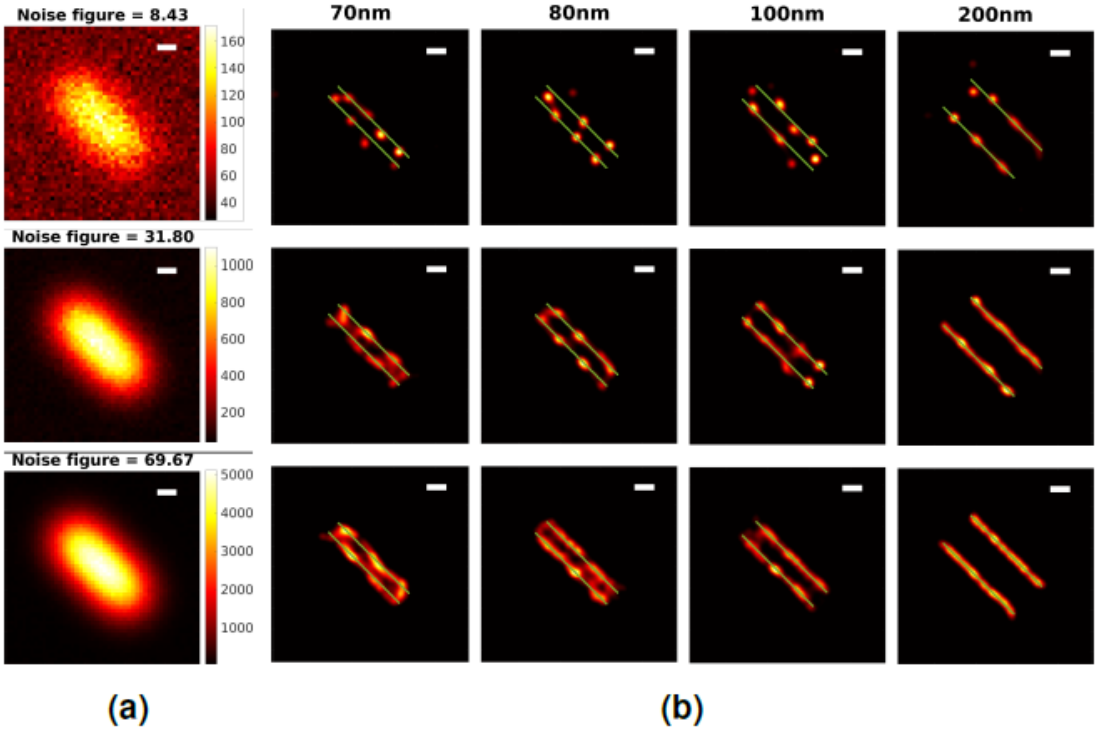

Fig. 17. Results of applying SUPPOSe to the synthetic image dataset. a Some of the synthetic images processed by varying the noise level present in them. b SUPPOSe results obtained after processing the synthetic images, increasing the separation distance between lines (from left to right) and the signal-to noise ratio in the image (from top to bottom). In green, the ground truth structure superimposed on each of the images. Scale bar is 100 nm.

The additional advantage of analyzing synthetic images is that the noise can be subtracted or filtered. In this manner it could be shown that the SUPPOSe algorithm is very robust against high frequency noise while low frequency noise can give rise to artifacts in the reconstruction, as shown in figure 18.
The comparison between repeated fits for similar images and the ground truth allowed a quantitative characterization of the accuracy of the method, and a similar comparison between fits determines the precision of the method. Due to the statistical nature of noise, the resolution cannot be determined in an absolute manner but instead the success rate of distinction between structures (lines in our case) is an indication of the resolution achievable under different noise figures. The results after repeated simulations are shown in figure 19

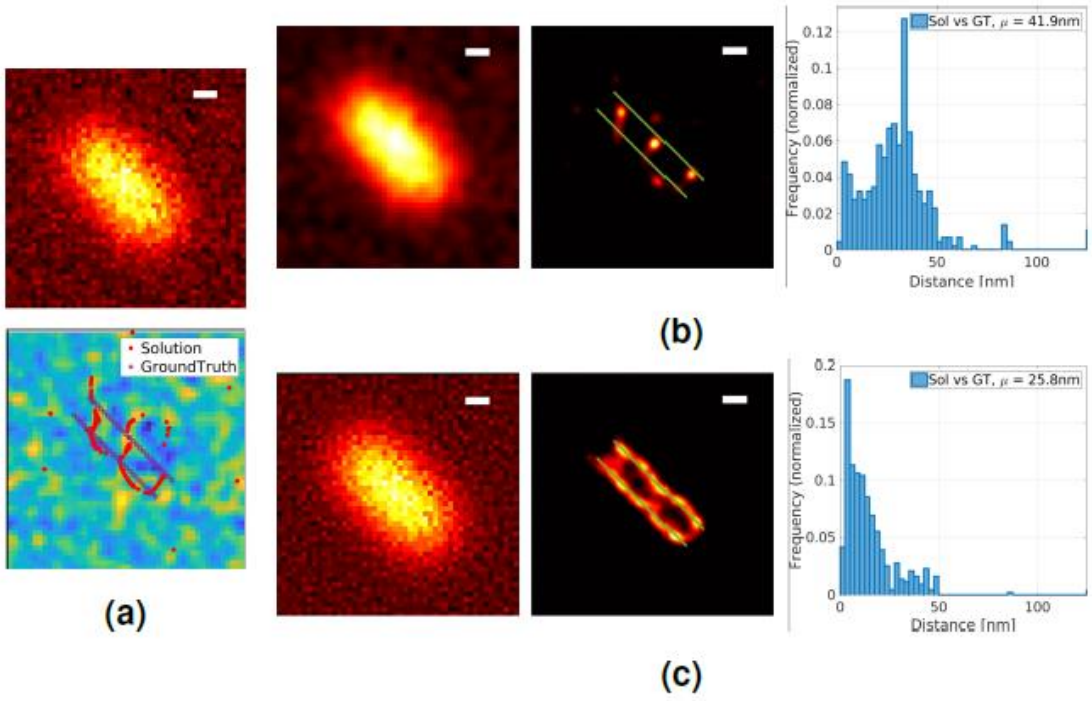

Fig. 18. Analysis of noise components and SUPPOSe solutions for synthetic images with lines separated by 100nm and NF = 9 (corresponding to maximum intensities in the image of 100 counts). a Original roi image (top). Coordinates of the virtual sources of the obtained solution superimposed on the low-frequency noise image (bottom). b SUPPOSe results obtained after processing the image without high-frequency noise components. c SUPPOSe results obtained after processing the image without low-frequency noise components. From left to right, the processed image, the solution obtained and the distance measurement between the solution and the ground truth structure. Scale bar is 100 nm.

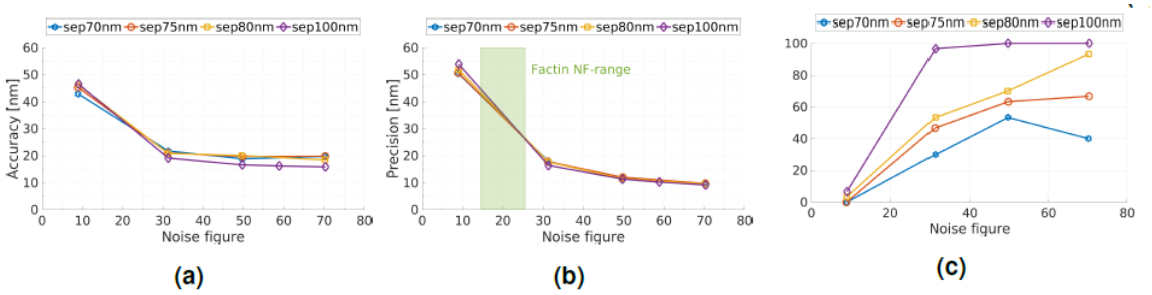

Fig. 19. Results of precision, accuracy and resolution rate for the set of processed synthetic images.

For more details see [29]

V-Super-resolved edge detection in 2D

A new approach to the edge detection problem is presented which is specially designed to achieve high accuracy detection, below instrumental resolution (super resolution) in microscopy images. The method is based in a modified version of the SUPPOSe algorithm [26-28]. The method was tested in simulated and experimental optical microscopy images and compared to the standard edge detection algorithms[30-32] , showing huge differences when the size of the object is smaller than the lateral resolution provided by the instrument.
The Suppose method proved to enhance resolution of wide-field fluorescence images up to four times. The resolution enhancement and the convergence speed of the algorithm is better when the image is sparse. This means that, in an application where we only need to identify the edges of a non sparse image, a lot of virtual sources (i.e. a large N) must be used to account for the parts of the image with no useful information. This results in a poor reconstruction.
The Edge Suppose algorithm overcomes this problem by fitting the gradient of the image, which is sparse for the images of interest. This brings increased complexity, as we should now reconstruct a vector field instead of an image. Computing the gradient in equation 1 we obtain

$$\nabla S = \nabla R * I + \eta', \qquad (7)$$

where η' is the derivative of the noise. ∇R' should only be large at the edges of the image, where a large leap in the intensity is present. Then, we want to approximate ∇R' as a superposition of point sources (sources of gradient rather than intensity), but this time we have to account for the direction of the gradient, i.e. the vector normal to the contour curve. Then we propose to approximate ∇R' as

$$\nabla R = \alpha \sum_{k=1}^{N_s} \delta(x - a_k, y - b_k)\hat{n}_k, \qquad (8)$$

Where $\hat{n}_k$ is the unit length normal vector, computed from the positions of the first neighbours of each source. Then we should minimize

$$\chi^2 = \|\nabla S - \nabla R * I\|^2 = \sum_{d=1}^{2} \sum_{i=1}^{N_x} \sum_{j=1}^{N_y} \left(\left((\nabla S)_{ij} - \alpha \sum_{k=1}^{N_s} I_{ij}^k \hat{n}_k \right) \cdot \hat{e}_d \right)^2, \quad (9)$$

At this point the problem is not well conditioned, as for example two sources placed at the same position but with opposite normal vector cancel out their contribution. For this reason a regularization term must be used to avoid rapid changes in the normal of the curve. Then we define the fitness *f* as

$$f = \chi^2 + \lambda \sum_{k=1}^{N_s} (1 - \hat{n}_k \cdot \hat{n}_{k+1})^2, \quad (10)$$

where λ is a parameter to choose in the algorithm.

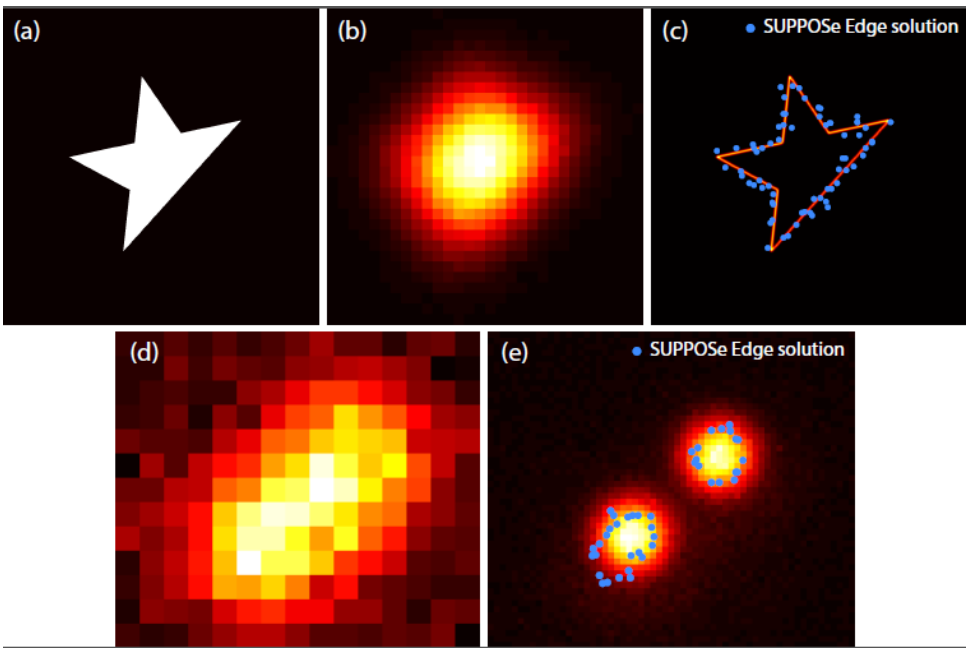

Figure 20. (a) Truncated star shaped object used to synthesize an artificial image. (b) Image after convolving the star with the microscope PSF and adding noise. (c) Ground truth edge (orange), reconstructed edge (blue dots). (d) Image of fluorescent beads with a 10x objective. (e) Reconstruction overlapped with a 40x objective image.

In figure 20 some examples of the results obtained with this new fitting function are shown. The upper one is a synthetic truncated star used to validate the method. It shows how a structure beyond the resolution of the microscope and apparently completely lost in the wide field image is recovered using this modified SUPPPOSe algorithm. The lower image shows a fluorescent microscopy frame of two closely

located beads taken with a low magnification objective and how the algorithm is able to separate the two beads as well as a high magnification (higher numerical aperture) objective. This result validates the method showing a threefold improvement in the instrument resolution.
More detailed results are presented in [33].

VI-3D reconstruction

In a SUPPOSe run, numerous convolutions are calculated, representing more than 90% of the computation time. By taking SUPPOSe to 3D, these times become prohibitive. To carry out this work we developed the CaTMU library [34], programmed in Python and CUDA, which performs the convolution in an optimized way, parallelizing the work in the thousands of cores of one (or multiple) GPUs. CaTMU also allows to work with PSFs defined by data table (LUT), and in this case, the texture mapping units are used, a component of the GPU with dedicated high-speed hardware, thus maximizing performance.

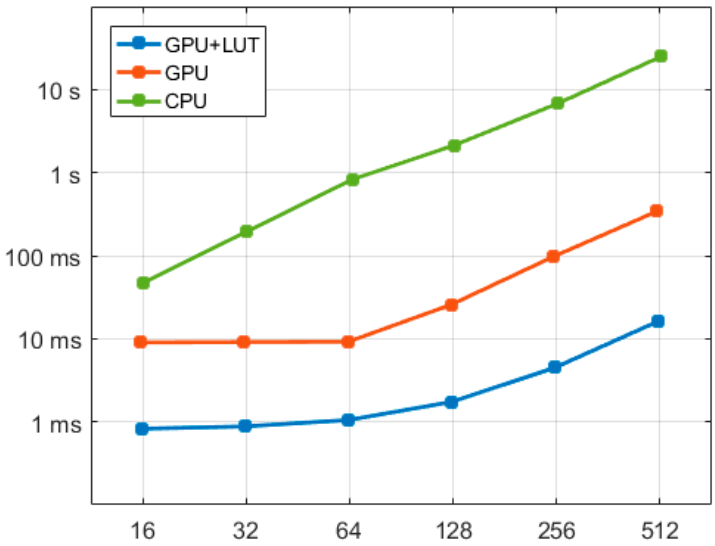

Figure 21. Computation time vs image size (in pixels per side) for CPU processing, GPU processing and GPU processing using the texture tools and look up tables for the PSF

The synthetic structure chosen for the 3D reconstruction was made of two lines located perpendicular to each other in the XY plane but displaced in the Z direction, as shown in figure 22. The solution obtained is shown in figure 23, where 200 virtual sources were used. The super-resolved structure was clearly recovered after processing. The metrics for the reconstructed images as compared to ground truth (accuracy) is shown in the histograms of figure 24.

These results have not been published yet.

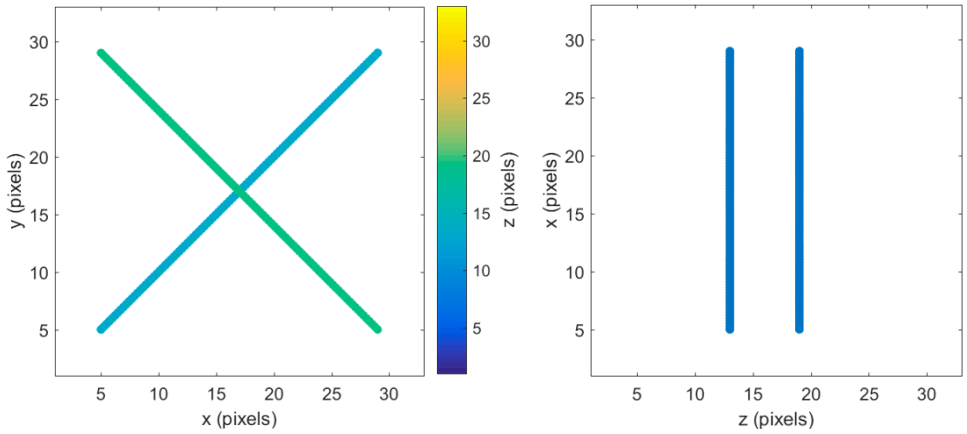

Figure 22. Left: Axial view, right : lateral view of the two lines.

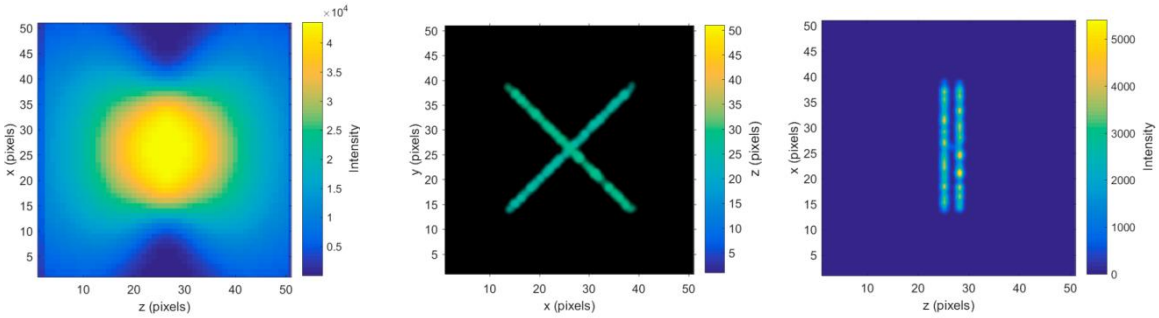

Figure 23. Case where lines were separated by the lateral PSF standard deviation. Left: synthetic image (lateral view). Middle: retrieved structure (axial view). Right: retrieved structure (lateral view).

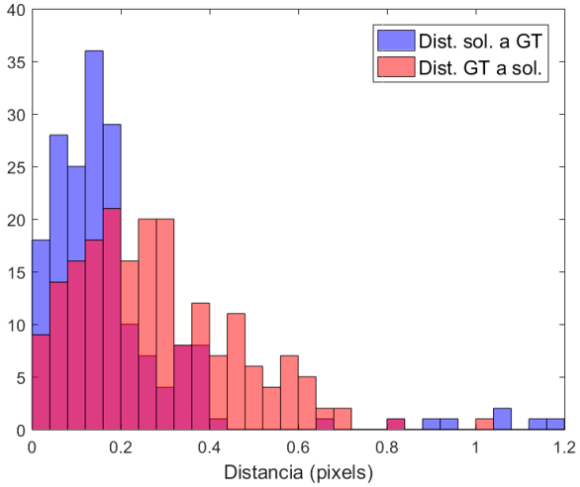

Figure 24. Histogram of the comparison between the solution and the ground truth (blue) and the ground truth to the solution (pink).

The other case in which 3D reconstruction was obtained is in the generalization of the edge detection method to the case of determining the surface of 3D objects. In figure 25 the triangular surface elements used for the surface construction is presented. The new chi square for the gradient is

$$\chi^2 = \|\nabla S - \nabla \tilde{R} * I\|^2 = \sum_{d=1}^{3} \sum_{i=1}^{P_x} \sum_{j=1}^{P_y} \sum_{k=1}^{P_z} \left(\left((\nabla S)_{ijk} - \alpha \sum_{t=1}^{N} I^t_{ijk} \hat{n}_t \right) \cdot \hat{e}_d \right)^2 \quad (11)$$

And the regularization term is now

$$\Lambda = \lambda \sum_{s=1}^{N_s} (\hat{n}_{s,1} \cdot \hat{n}_{s,2} - 1)^2 \quad (12)$$

And the fitness function results

$$f = \chi^2 + \Lambda. \quad (13)$$

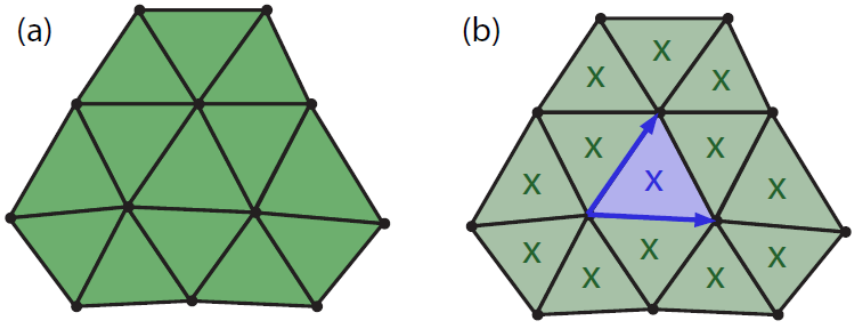

Figure 25 Surface representation for the SUPPOSe 3Dge algorithm. (a) V ertices and triangular faces that form the surface. (b) Virtual sources of SUPPOSe (x). Vectors nen blue (from its cross product) the direction of the normal corresponding to the highlighted face.

One example of the 3D reconstruction with this version (called SUPPOSe 3Dge) is shown in figure 26 where a star smaller than the PSF is recovered with great detail, as compared with the failure of other edge detection techniques. The metric also shows a very good accuracy in the reconstruction.
These results are part of the PhD thesis of Guillermo Brinatti Vazquez, and have not been published yet.

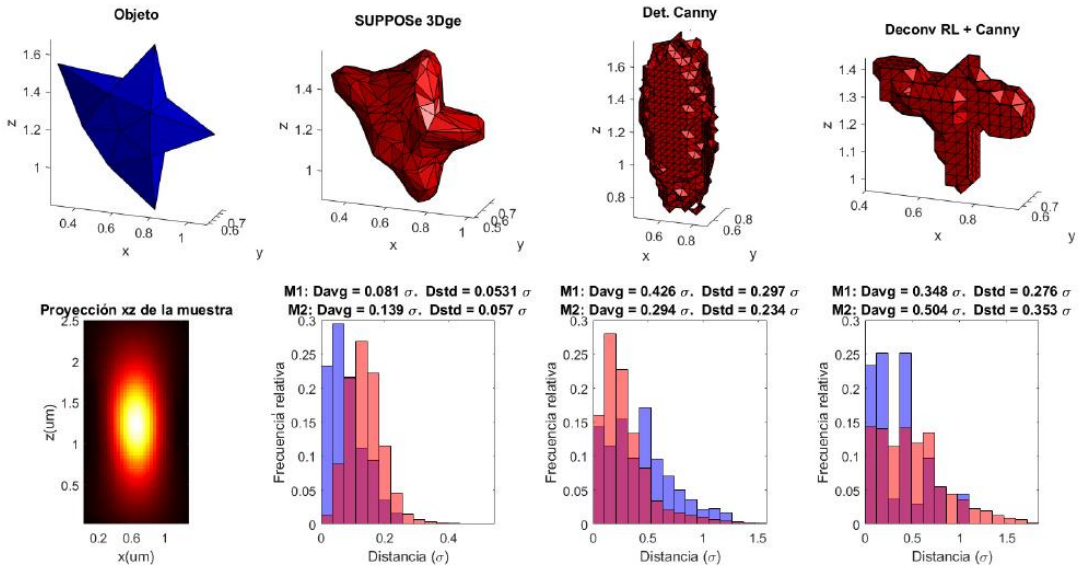

Figure 26. SUPPOSe 3Dge solution for a star smaller than the PSF. Row top (respectively): high resolution sample, SUPPOSe 3Dge solution,Canny edges and Canny edge detection after image deconvolution by Richardson Lucy. Bottom row (respectively): projection xz of the simulated volumetric image), then, each histogram corresponds to the distance metrics of the upper solution

VII- Scattering imaging

An important step in this project was to extend the SUPPOSe method beyond fluorescent microscopy. One of the requisites is that the image is formed by incoherent superposition of the contribution from each point of the object. Scattering with incoherent illumination appeared as a promising scenario.
As the method performs particularly well with low dimensionality of the object, structures with relief illuminated with grazing incident light (dark field illumination) where found especially adequate for the experiment.
The sample used consisted in structures engraved by lithography on a crystalline silicon substrate with a 1nm oxide layer and a 150nm thick polycrystalline silicon layer on top. This top layer was etched by UV lithographic methods obtaining very small strcutures that cannot be resolved by the optical microscope.
In figures 27 and 28 two examples are presented showing the super-resolution apparently obtained. Unfortunately due to the pandemic the scanning electron microscope has not been operative the last two years and we could not calibrate the size and shape of the structures to validate the retrieved structures.
Work is in progress to continue with this promising line.

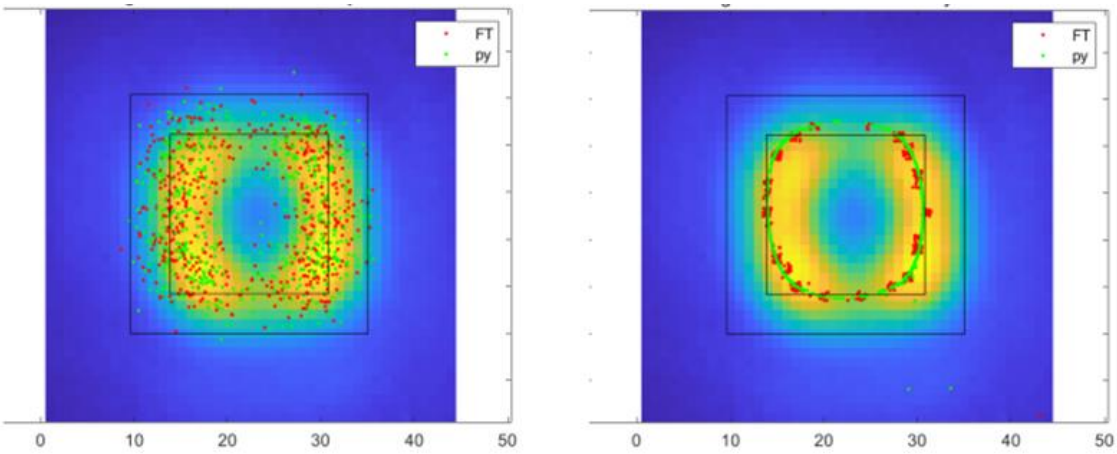

Figure 27 Sample nominally shaped as squares 600nm wide. The black squares are for scaling and are 1000nm and 667nm wide. Left Measured image and scattered initial positions for the sources. Right: retrieved solution overlapped with the measured signal. Red: SUPPOSe_fft, green: standard SUPPOSe

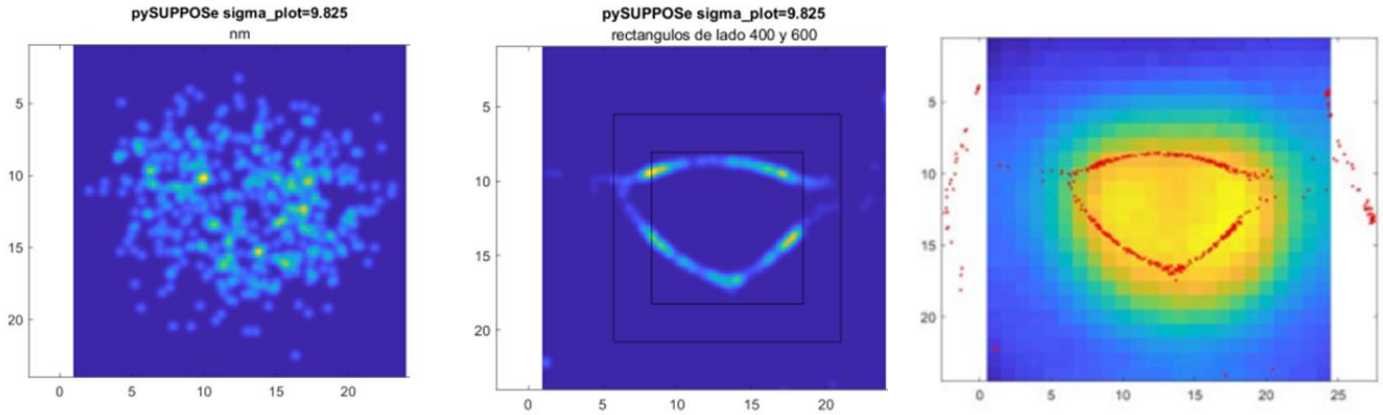

Figure 28 Sample nominally shaped as squares 400nm wide. The retrieved structure does not resemble the nominal shape but as the size is too small for the fabrication technique, failure from the designed shape is expected. SEM images should be performed whenm available for cross checking. Black squares are 400nm and 600nm wide.

VIII-Adding Artificial Intelligence for noise reduction

We have developed gSUPPOSe, a new and faster version of SUPPOSe that allows for the localization of multiple overlapped emitters (i.e. high fluorophore densities) in continuous space and under arbitrary (theoretical or experimental) PSF models. We have used gSUPPOSe and CS-STORM for single emitter lo calization at high fluorophore densities (i.e. overlapping PSFs) in simulated samples with low- and high-SNR. To this purpose, we generated a sample dataset available at [35] that comprises three different fluorophore geometries at different distances, SNR conditions and multiple noise realizations, and we also propose a

new method to localize the emitters from SUPPOSe and CS solutions. Our results have shown that gSUPPOSe outperforms CS-STORM for low-SNR images, providing better localization error and resolving all the emitters for SNR values down to one order of magnitude less than the required for CS-STORM. At high SNR conditions both methods performed similar, with CS being more precise but having an asymptotically decreasing bias. gSUPPOSe is written in Python and uses an additional library to enhance computational speed through distributed computing acceleration in both CPU and GPU. The code of both libraries are available at [36] and [34].

We have also studied image denoising with a deep convoutional network as a pre-processing stage for SNR-improved emitter localization. By using a physical model for image formation, we have trained the network proposed in [37] with a simulated dataset as a way to overcome the limited experimental data that is usually available. This model increased the SNR of our images by a factor larger than 2 by removing noise at frequencies similar to and higher than the PSF frequency cutoff. We have demonstrated that this pre-processing greatly enhances CS localizations, extending the SNR range where the method is valid down to values similar to the ones of SUPPOSe. In the other hand, image denoising only improved SUPPOSe localizations by slightly reducing the localization error, indicating that SUPPOSe is inherently less affected by mid- and high-frequency noise. The combination of single-molecule localization with prior sample denoising by means of deep learning methods that rely on physical information, such as specific image formation and noise models, may greatly benefit the performance of other algorithms used in the SMLM community.

Some of the results of the noise suppression using the neural network are shown in figure 29. For different noise figures (different maximum intensity i_{max}), and different source configurations the synthetic images were generated in a repeated manner to obtain different noise realizations with the same noise figure. Some of the results are shown in figure 30 where the retrieved solution is shown with and without noise reduction for compressed sensing algorithm and SUPPOSe algorithm.

For more details see [38]

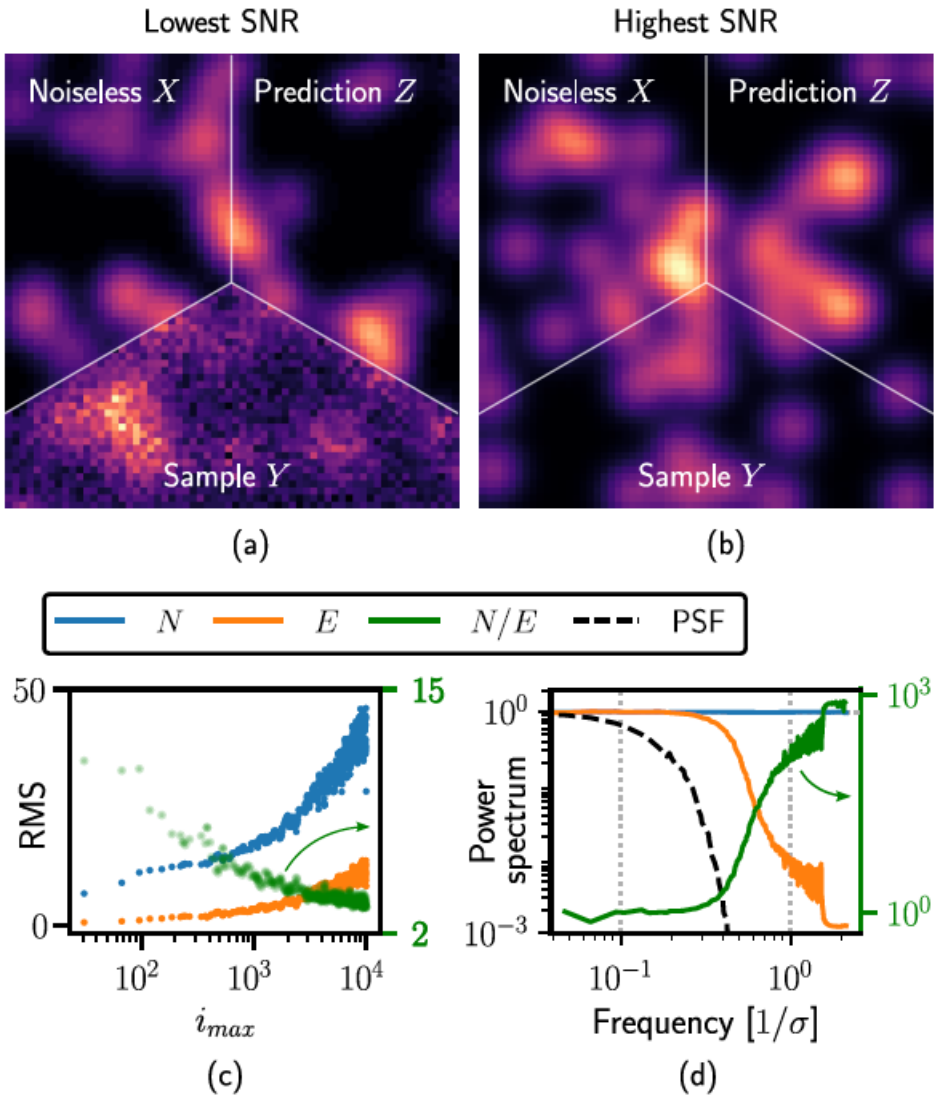

Figure 29. (Color online) Performance of the denoising model f over the secondary train dataset. Figures (a) and (b) illustrates the denoising process for two sets of validation images with low and high SNR respectively. Figure (c) evaluates the model in real space, showing RMS values of noise N, prediction error E (left axis) and the improvement ratio N/E (right axis) as a function of SNR. Figure (d) evaluates the model in frequency space, showing the power spectrum of N, E (left axis) and the improvement ratio N/E (right axis) averaged over the whole validation subset (including all imax). The normalized PSF power spectrum is also shown to compare with the frequency cutoff 1/σ.

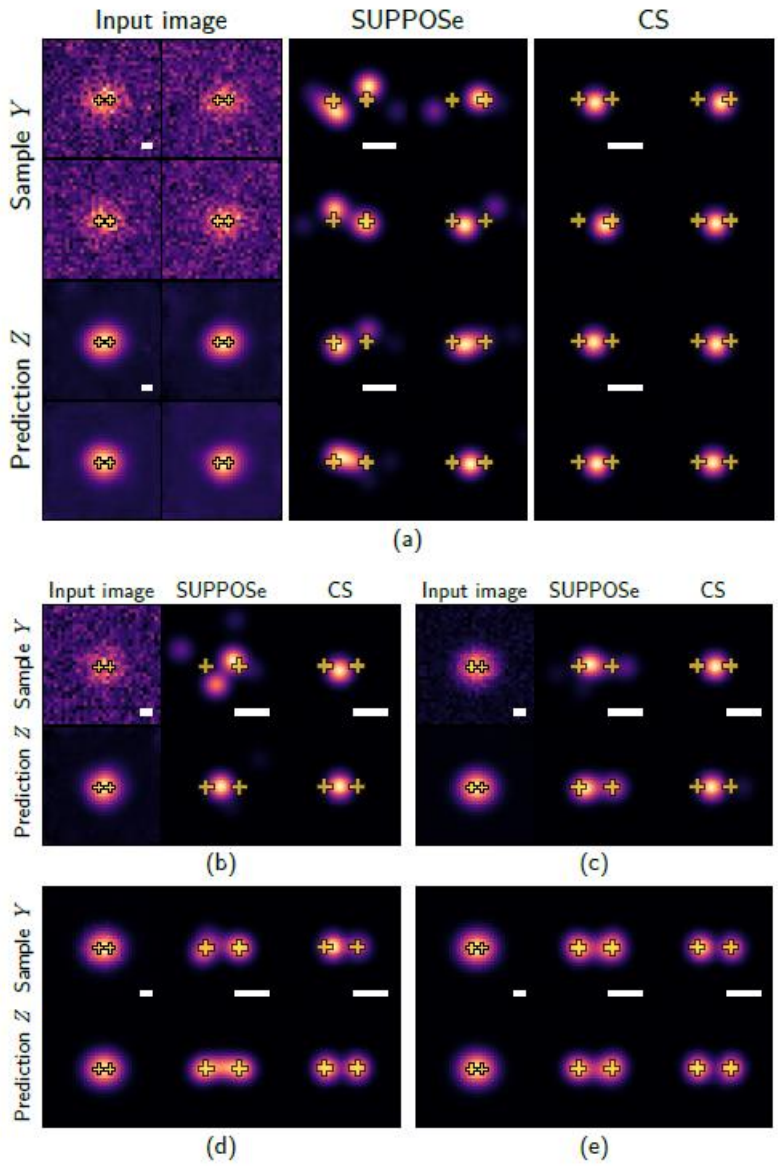

Figure 30. (Color online) Results of SUPPOSe and CS for Q =2 true emitters separated at d =1.0σ. In the upper half figure (a) we show the results for four samples Y (same configuration, different noise realizations) and their corresponding denoised images Z. In the lower half we show similar results for only one noise realization and increasing SNR: (a) imax = 20, (b) imax = 108, (c) imax = 1043 and (d) imax = 10 000. The true emitters are shown as yellow crosses. In all cases, the length of the scale bar σ.

Conclusions

A new method has been developed that opens the field of super-resolution microscopy to standard equipment and single shot experiments. In this manner fast events can be traced with high spatial resolution never available before. This new method, SUPPOSe (for Superposition of point sources) is based on the assumption that the target object to be retrieved (hidden by the resolution of the

instrument) can be represented as the superposition of virtual sources of the same intensity. In this manner the ill posed mathematical problem of inverting the convolution (deconvolution) is converted to a well posed problem and a resolution beyond the instrument limitation can be achieved. The limits to this deconvolution are placed by the noise figure of the measurement and the precision with which the instrument response function is determined.

The method has been shown to work in the deconvolution of fluorescent images and artificially synthesized images and several improvements on the original algorithm were implemented resulting in faster and more reliable results. Among them was the shift to GPU processing, the use of look up tables for the definition of the PSF using textures in the GPU, a new fitting function based on the covariance instead of the chi squared that was then followed by a Fourier space implementation. Artifacts arising from sources close to the edge of the frame were also corrected.

In the seminal paper [25] detailed mathematical derivations showed which are the main limitation sources: precision in the measurement of the PSF, noise and truncation due to the finite number of virtual sources. It was proved that the reformulated deconvolution problem is now well posed, but the analytical bounds for the quality of the reconstruction were too coarse. Hence detailed and systematic studies of the accuracy, precision and resolution of the method were carried out to ascertain up to what level the retrieved structures are reliable. Resolutions down to 70nm, with accuracies of 20nm and precisions down to 10nm were shown possible with standard optical microscopes.

It was shown up to what extent the main limitation is noise in the acquisition process, and AI methods based on neural networks were implemented to reduce the noise for the case of sparse objects.

The method is being extended to standard scattering images, not requiring fluorescent markers, which will result in a fantastic jump for super-resolution microscopy.

Work in progress involves the extension to coherent imageing, applications to medical instrumentation such as Optical Coherent Tomography, and extending the method to other instrumentations such as mass spectroscopy and material science.

From the work describe in this report two PhD thesis were completed (Micaela Toscany and Guillermo Brinatti Vazquez).

References

1-Hell, S. W.; Wichmann, J. (1994). "Breaking the diffraction resolution limit by stimulated emission: Stimulated-emission-depletion fluorescence microscopy". Optics Letters. 19 (11): 780–782. Bibcode:1994OptL...19..780H. doi:10.1364/OL.19.000780. PMID 19844443.

2- Westphal, V.; S. O. Rizzoli; M. A. Lauterbach; D. Kamin; R. Jahn; S. W. Hell (2008). "Video-Rate Far-Field Optical Nanoscopy Dissects Synaptic Vesicle Movement". Science. 320 (5873): 246–249. Bibcode:2008Sci...320..246W.

3- Betzig, E., Patterson, G.H., Sougrat, R. et al. (2006) Imaging intracellular fluorescent proteins at nanometer resolution. Science 313(5793), 1642–1645.

4- Hess, S.T., Girirajan, T.P.K. & Mason, M.D. (2006) Ultra-high resolution imaging by fluorescence photoactivation localization microscopy. Biophys. J, 91(11), 4258–4272.

5- Rust, M.J., Bates, M. & Zhuang, X. (2006) Sub-diffraction-limit imaging by stochastic optical reconstruction microscopy (storm). Nat. Methods 3(10), 793–796.

6- McNally, J.G., Karpova, T., Cooper, J. & Conchello, J.A. (2006) Threedimensional imaging by deconvolution microscopy. Methods 19(3), 373–385.

7- Erhardt, A., Zinser, G., Komitowski, D. & Bille, J. (1985) Reconstructing 3-d light-microscopic images by digital image processing. Appl. Opt. 24(2), 194–200.

8- Tommasi, T., Diaspro, A.&Bianco, B. (1993) 3-d reconstruction in optical microscopy by a frequency-domain approach. Signal Process. 32(3), 357–366.

9- Voort, H.T.M.V.D. & Strasters, K.C. (1995) Restoration of confocal images for quantitative image analysis. J. Microsc. 178(2), 165–181.

10- Kempen, G.M.P.V., Vliet, L.J.V., Verveer, P.J. & Voort, H.T.M.V.D. (1997) A quantitative comparison of image restoration methods for confocal microscopy. J. Microsc. 185(3), 354–365.

11- Verveer, P.J. & Jovin, T.M. (1997) Acceleration of the ictm image restoration algorithm. J. Microsc. 188(3), 191–195.

12- de Monvel, J.B., Calvez, S.L. & Ulfendahl, M. (2001) Image restoration for confocalmicroscopy: improving the limits of deconvolution, with application to the visualization of the mammalian hearing organ. Biophys. J. 80(5), 2455–2470.

13- Beck, A. & Teboulle, M. (2009) A fast iterative shrinkage-thresholding algorithm for linear inverse problems. SIAM J. Imaging Sci. 2(1), 183– 202.

14- Sage, D., Donati, L., Soulez, F. et al. (2017) Deconvolutionlab2: An opensource software for deconvolution microscopy. Methods 115, 28–41.

15- Donoho, D.L. (1992) Superresolution via sparsity constraints. SIAM J. Math. Anal. 23(5), 1309–1331.

16- Cand`es, E.J., Romberg, J. & Tao, T. (2006) Robust uncertainty principles: exact signal reconstruction from highly incomplete frequency information. IEEE Trans. Inf. Theory 52(2), 489–509.

17- Morgenshtern, V.I. & Cand`es, E.J. (2016) Super-resolution of positive sources: the discrete setup. SIAM J. Imaging Sci. 9(1), 412–444.

18- Ekanadham, C., Tranchina, D. & Simoncelli, E.P. (2011) Recovery of sparse translation-invariant signals with continuous basis pursuit. IEEE Trans. Signal Process. 59(10), 4735–4744.

19- Zhu, L., Zhang, W., Elnatan, D. & Huang, B. (2012) Faster storm using compressed sensing. Nat. Methods 9(7), 721–723.

20- Chouzenoux, E., Pesquet, J.-C. & Florescu, A. (2014) A multi-parameter optimization approach for complex continuous sparse modelling. In 2014 International Conference on Digital Signal Processing (DSP), 20–23 August 2014, Hong Kong, China.

21- Duval, V. & Peyr´e, G. (2015) Exact support recovery for sparse spikes deconvolution. Found. Comput. Math. 15(5), 1315–1355.

22- Min, J., Vonesch, C., Kirshner, H. et al. (2014) Falcon: fast and unbiased reconstruction of high-density super-resolution microscopy data. Sci. Rep., 4, 4577.

23- Hugelier, S., Eilers, P., Devos, O. & Ruckebusch, C. (2017) Improved superresolution microscopy imaging by sparse deconvolution with an interframe penalty. Jo. Chemometr. 31(4), e2847.

24- Hugelier, S., De Rooi, J., Bernex, R. et al. (2016) Sparse deconvolution of high- density super-resolution images open. Scientific Reports, 6, 1–10.

25- Martínez, S., Toscani, M., Martinez, O.E. Superresolution method for a single wide-field image deconvolution by superposition of point sources. Journal of Microscopy 275(1), pp. 51-65. 2019

26- Toscani, M., Martínez, S., Martínez, O.E. Single image deconvolution with super-resolution using the SUPPOSe algorithm. Progress in Biomedical Optics and Imaging - Proceedings of SPIE 10884,1088415. 2019

27- M. Toscani and S. Martínez, "Solving the boundary artifact for the enhanced deconvolution algorithm suppose applied to fluorescence microscopy," Computer Optics, vol. 45, no. 3, pp. 418–426, 2021.

28-Lacapmesure, A.M., Martínez, S., Martínez, O.E. "A new objective function for super-resolution deconvolution of microscopy images by means of a genetic algorithm", GECCO 2020 Companion - Proceedings of the 2020 Genetic and Evolutionary Computation Conference Companion, 2020, pp. 271–272

29- Toscani, M., Martínez, O.E.., Martínez, S. "Resolution, accuracy and precision in super-resolved microscopy images using SUPPOSe" Sent to Optics Letters, 2021

30- J. Kaur, S. Agrawal, and R. Vig, "A comparative analysis of thresholding and edge detection segmentation techniques," Int. J. computer applications 39, 29–34 (2012).

31- J. Canny, "A computational approach to edge detection," IEEE Transactions on pattern analysis machine intelligence. pp. 679–698 (1986).

32- D. Marr and E. Hildreth, "Theory of edge detection," Proc. Royal Soc. London. Ser. B. Biol. Sci. 207, 187–217 (1980).

33- Brinatti Vazquez, G. D., Martínez, S. and Martínez O. E., Super-resolved edge detection in optical microscopy images by superposition of virtual point sources, Opt. Express 28, 25319-25334 (2020). https://doi.org/10.1364/OE.397125

34- A. Mazzeo, "CaTMU repository," (2021). https://github.com/alemazzeo/catmu.

35- Datasets used (2021) http://dx.doi.org/10.5281/zenodo.5528368

36- A. M. Lacapmesure, "gSUPPOSe repository," (2021). https://gitlab.com/labofotonica/gsuppose.

37- M. Weigert, and many "Content-aware image restoration: pushing the limits of fluorescence microscopy," Nat. Methods 15, 1090–1097 (2018).

38- Lacapmesure, A. M. , A Brinatti Vazquez, G. D., Mazzeo, A. Martínez, S. and Martínez O. E "Combining deep learning with SUPPOSe and Compressed Sensing for SNR-enhanced localization of overlapping emitters" Sent to Applied Optics 2021.

List of Symbols, Abbreviations and Acronyms

λ: regularization parameter for edge detection (or eventually wavelength)
$\eta(x)$: noise
η': derivative of the noise
a_k :positions of the sources.
B(x): background
BPAEC: bovine pulmonary artery endothelial cells
I(x). PSF
N: number of virtual sources
NF: noise figure
$\hat{n}_k$. unit length normal vecto
R(x): actual source term to be determined
R´: reconstructed source term
S(x); measurement (image)
S´: reconstructed image
x: coordinate in the image
GPU: graphical processing unit
NA: numerical aperture
PALM:
PSF: Point spread function
SEM: scanning electron microscope
STED
STORM
SUPPOSe: superposition of point sources: the developed algorithm.